Diverging responses of high-latitude CO_2 and CH_4 emissions in idealized climate change scenarios

Philipp de Vrese[1], Tobias Stacke[2], Thomas Kleinen[1], and Victor Brovkin[1,3]

[1]Max Planck Institute for Meteorology, The Land in the Earth System, Hamburg, 20146, Germany
[2]Helmholtz-Zentrum Geesthacht, Institute of Coastal Research, Geesthacht, 21502, Germany
[3]University of Hamburg, Center for Earth System Research and Sustainability, Hamburg, 20146, Germany

Correspondence: Philipp de Vrese (philipp.de-vrese@mpimet-mpg.de)

Abstract. The present study investigates the response of the high latitude's carbon cycle to in- and decreasing atmospheric greenhouse gas (GHG) concentrations in idealized climate change scenarios. To this end, we use an adapted version of JSBACH – the land-surface component of the Max-Planck-Institute for Meteorology's Earth system model (MPI-ESM) – that accounts for the organic matter stored in the permafrost affected soils of the high northern latitudes. To force the model, we use different

5   climate scenarios that assume an increase in GHG concentrations, based on the Shared Socioeconomic Pathway 5 and the Representative Concentration Pathway 8.5, until peaks in the years 2025, 2050, 2075 or 2100, respectively. The peaks are followed by a decrease in atmospheric GHGs that returns the concentrations to the levels at the beginning of the 21st century. We show that the soil CO_2 emissions exhibit an almost linear dependency on the global mean surface temperatures that are simulated for the different climate scenarios. Here, each degree of warming increases the fluxes by, very roughly, 50% of

10 their initial value, while each degree of cooling decreases them correspondingly. However, the linear dependency does not mean that the processes governing the soil CO_2 emissions are fully reversible on short timescales, but rather that two strongly hysteretic factors offset each other – namely the vegetation's net primary productivity and the availability of formerly frozen soil organic matter. In contrast, the soil methane emissions show almost no increase with rising temperatures and they are consistently lower after than prior to a peak in the GHG concentrations. Here, the fluxes can even become negative and we

15 find that methane emissions will play only a minor role in the northern high latitudes' contribution to global warming, even when considering the gas's high global warming potential. Finally, we find that the high-latitude ecosystem acts as a source of atmospheric CO_2 rather than a sink, with the net fluxes into the atmosphere increasing substantially with rising atmospheric GHG concentrations. This is very different to scenario simulations with the standard version of the MPI-ESM in which the region continues to take up atmospheric CO_2 throughout the entire 21st century, confirming that the omission of permafrost-

20 related processes and the organic matter stored in the frozen soils leads to a fundamental misrepresentation of the carbon dynamics in the Arctic.

1   Introduction

High-latitude terrestrial ecosystems are recognised as an increasingly important factor for the global carbon cycle. On the one hand, global warming is expected to increase the vegetation cover and primary productivity – a trend termed Arctic greening (Keenan and Riley, 2018; Pearson et al., 2013; Zhang et al., 2018), which could significantly increases the terrestrial uptake of atmospheric CO_2 (Qian et al., 2010; McGuire et al., 2018). On the other hand, there are large quantities of effectively inert organic matter stored within the frozen soils of the Northern Hemisphere and a significant fraction of these could become exposed to microbial decomposition in a warmer climate. Areas underlain by permafrost – defined by soil temperatures below the freezing point for at least 2 consecutive years – contain between 1100 - 1700 Gt of carbon, the largest fraction of which is stored within the frozen part of the ground (Zimov, 2006a; Tarnocai et al., 2009; Hugelius et al., 2014). With the temperature increase in the high-latitudes being about twice as large as the global average (Stocker et al., 2013), the last decades have already seen substantial changes in the permafrost-affected regions. Regional soil temperatures have increased by up to 2 K and there is a pronounced retreat in the extent of permafrost-affected areas combined with an increase in active layer depth, which leaves large quantities of organic matter vulnerable to decomposition (Biskaborn et al., 2019; Stocker et al., 2013; Etzelmueller et al., 2011; Osterkamp, 2007; Shiklomanov et al., 2010; Frauenfeld, 2004; Wu and Zhang, 2010; Callaghan et al., 2010; Isaksen et al., 2007; Brown and Romanovsky, 2008; Romanovsky et al., 2010).

Climate change scenarios project the artic temperatures to increase by between 3 K and 8 K until the end of the 21st century (Stocker et al., 2013). Many modelling studies have investigated the resulting decrease in organic matter stored in the permafrost-affected regions and, for the high emission scenarios – corresponding to a temperature increase of 8 K –, the soils are expected to emit around 120 ± 80 Gt of carbon until the year 2100 (Schuur et al., 2013; Schaefer et al., 2014; McGuire et al., 2018). Increasing temperatures also accelerate the Arctic greening trend and it is highly uncertain at which point the carbon release from thawing soils would surpass the additional carbon uptake by vegetation. However, it is generally assumed that the artic ecosystem will turn from a carbon sink into a carbon source within the 21st century (Schaefer et al., 2011; Schuur et al., 2015). The (net) carbon release will further increase the atmospheric greenhouse gas (GHG) concentrations, leading to a positive feedback. Studies indicate, that this feedback will not only notably accelerate the global warming for high emission scenarios – which result in a near-disappearance of the terrestrial near-surface permafrost – but even for the temperature-target of the Paris Agreement (MacDougall et al., 2012; Burke et al., 2017b, 2018; Comyn-Platt et al., 2018).

It is exceedingly difficult to estimate the Arctic's contribution to future warming. One issue is the timescale on which the carbon would be released from permafrost-affect soils. While local observations indicate that the change processes, affecting the soil carbon emissions, are locally confined and act on very short timescales, large scale modelling studies suggest that the increase in emissions is likely to occur gradually over a timescale of hundreds of years (Schuur et al., 2015). Another important issue is the fraction of carbon that is released in the form of CH_4 rather than CO_2. Methane is a much more potent GHG (Stocker et al., 2013), and even a small fraction of formerly frozen carbon that is released as CH_4 would increase the respec-

tive global warming potential substantially. Methane is produced during the decomposition under anaerobic conditions and these require soils to be water saturated. Hence, future methane emissions are highly dependant on changes in the sub-surface hydrology in permafrost-affected regions (Olefeldt et al., 2012). It is difficult to represent saturated soils at the typical spatial resolution of present-day Earth system models, making it hard to determine the areas in which the decomposition occurs under anaerobic conditions. Furthermore, the hydrological response to permafrost degradation is very complex and there is some disagreement between land-surface models even as to whether high-latitude soils would in general become drier or wetter in the future (Berg et al., 2017; Andresen et al., 2019). Thus, there are comparatively few studies that use large-scale models to investigate the change in soil methane emissions for future warming scenarios (Lawrence et al., 2015; Burke et al., 2012; von Deimling et al., 2012; Koven et al., 2015; Oh et al., 2020).

The present study aims to improve our understanding of the arctic ecosystem's importance for the global carbon cycle not only by providing additional estimates of the carbon fluxes under a future warming scenario. More importantly, the study's goal is to provide a better understanding of the processes that govern these fluxes – in particular the soil methane emissions – in permafrost-affected regions. The current anthropogenic GHG emissions make it increasingly likely that temperatures will overshoot any temperature target, before atmospheric GHG concentrations could be stabilized at a desirable level (Geden and Löschel, 2017; Parry et al., 2009; Huntingford and Lowe, 2007; Nusbaumer and Matsumoto, 2008). But while many studies have investigated the response of the arctic ecosystem to increasing GHG concentrations, only a few studies exist that investigate its response to a decrease in concentrations (Boucher et al., 2012; Eliseev et al., 2013) and it is still an open question how the high-latitude carbon cycle responds to overshooting temperatures. Thus, we do not only target the system's response to increasing temperatures, but also during a consecutive temperature decline.

Our investigation is based on simulations with the land-surface component of the MPI-ESM1.2 (Mauritsen et al., 2019), the latest release of the Max-Planck-Institute for Meteorology's Earth system model. However, we could not use the standard JSBACH model, as it includes certain parametrizations that are not well adapted to the specific conditions that are characteristic for high latitudes and neither does it account for freezing and melting of soil water, nor for the methane production in the soil. In the following we will describe the required modifications to the model, together with a more detailed description of the simulations that were performed in the context of this study (Sec. 2). Section 3 details our findings with respect to the soil CO_2 and CH_4 under in- and decreasing temperatures, while section 4 discusses them in the context of the global carbon cycle.

2 Methods

2.1 Model

The changes that were made to JSBACH include the implementation of 3 new modules that represent the formation of inundated areas (sec. 2.1.3) and wetlands (sec. 2.1.3) as well as the soil methane production including the gas-transport in soils (sec. 2.1.4).

Furthermore, we adapted the model's soil physics and carbon cycle to include the processes that are relevant for permafrost-
90 affected regions.

2.1.1 Soil carbon

In JSBACH, the soil carbon dynamics are simulated by the YASSO model, which calculates the decomposition of organic
matter at and below the surface considering five different lability classes –acid-hydrolyzable, water-soluble, ethanol-soluble,
non-soluble/non-hydrolyzable and a more recalcitrant humus pool (Liski et al., 2005; Tuomi et al., 2011). The decomposition
95 rates are determined by the standard mass loss parameter, which differs between the lability classes, and two factors that
account for the temperature and moisture dependencies of the decomposition process. The standard YASSO model does not
consider a vertical distribution of the organic matter within the soil and the decomposition rates depend on the simulated surface
temperatures, and precipitation rates. This approach works well in regions in which most of the soil carbon is stored close to the
surface, but it is problematic for permafrost-affected regions. The vertical carbon transport in these regions is dominated by very
100 effective processes – cryoturbation (Schuur et al., 2008) – and soils can store organic matter in depth of several meters. Thus, the
conditions under which this organic matter decomposes are not well approximated by surface temperatures and precipitation
rates. To improve the representation of the carbon cycle in permafrost-affected regions, we implemented a vertical structure
of the soil carbon pools and calculate the decomposition rates using depth dependant soil temperature and liquid soil water
content. Furthermore, we added a simple parametrization to distribute the carbon inputs according to idealized root-profiles
105 and a scheme to account for the accumulation of organic matter at the top of the soil column and the vertical transport due to
bio- and cryoturbation.

Structure of the soil carbon pools

JSBACH distinguishes between above and below ground carbon pools, a separation that is – in the standard model – only
relevant for the computation of the fuel load required by the model's fire module. However, fresh litter at the surface – such
110 as branches or leaves – has very different properties than organic matter that is encompassed in the soil. To be able to account
for these differences, the new structure maintains the separation of above and below ground carbon but introduces a vertical
discretization of the below ground carbon pools. As we also maintain the conceptual structure of the lability classes, the new
scheme represents soil carbon by 5 lability classes on every model soil layer and 4 above ground carbon pools (note that the
humus pool does not exist at the surface, see below).

115

The present model version distinguishes between anoxic and oxic decomposition in the inundated and the non-inundated
fractions of the grid box (see below) and the soil carbon pools need to be separated accordingly. Here, we do not simulate
the respective pools explicitly. Instead we calculate r_{cin}, the ratio between the carbon concentrations in the inundated and the
non-inundated fractions, for each of the soil carbon pools after the decomposition is computed. In the consecutive time step,
120 the soil carbon is distributed between inundated and non-inundated carbon pools according to r_{cin} before the decomposition is
calculated. For changes in the inundated area, r_{cin} is modified between two calls of the decomposition routine. This approach

allows us to separate oxic and anoxic respiration without having to calculate the entirety of relevant processes – such as land cover changes, disturbances, etc. – for two sets of carbon pools.

125   For technical reasons we chose to represent the soil carbon pools simultaneously on two different vertical resolutions (soil layers). The coarse layering corresponds to the one used to represent soil temperatures and the hydrological processes while the spacing of the finer layers can be chosen freely. The second structure was implemented because we found JSBACH's standard vertical resolution to be too coarse to properly represent the vertical mixing due to cryoturbation, while it is comparatively expensive to represent all soil processes on a fine grid.

130

Carbon inputs

In JSBACH, the litter inputs are divided into above and below ground litter fluxes, with 70% of the coarse and 50% of the fine litter entering the above ground pools. We maintain this separation but distribute the below ground litter inputs on the vertical soil layers according to vegetation type specific root profiles. Similarly, the below ground carbon inputs that result
135   from disturbances and land-use change as well as root exudates are distributed according to these profiles. The cumulative root fraction, Y, is described by:

$$Y = 1.0 - \beta^z, \tag{1}$$

with z being the depth below the surface. The parameter β is taken from Jackson et al. (1996) and matched to the plant functional types employed by JSBACH. Furthermore, the cumulative root fraction is scaled by a maximum depth, which is
140   limited by the lower of either the model's prescribed rooting depth or the previous year's maximum thaw depth. The latter is done because JSBACH uses a rooting depth that is fixed in each grid box, but we assume that plants do not extend their roots into the perennially frozen regions of the soil.

Transport

The vertical carbon transport in permafrost-affected regions is dominated by frost heave and freeze-thaw cycles (Schuur et al.,
145   2008). However, cryoturbation involves a variety of complex processes that depend on small scale features of the soil and, even though process models exists (Peterson et al., 2003; Nicolsky et al., 2008), these are not applicable on the scales of land-surface models. Thus, we follow the approach of Koven et al. (2009, 2013) and described the vertical mixing of soil organic matter as a diffusive transport:

$$\frac{\partial C_{lc,z}}{\partial t} = \frac{\partial}{\partial z} \left(D(z) \frac{\partial C_{lc}}{\partial z} \right), \tag{2}$$

150   with C being the carbon concentration of the lability class lc, D the diffusion coefficient and z the depth below the surface.

Similar to Burke et al. (2017a) we use a constant diffusivity – not varying between grid boxes– to represent bioturbation in regions that are not affected by near-surface permafrost. At the surface we use a diffusivity of 1.5 cm^2 year^{-1} and for the deeper layers we assume the mixing rates to decline linearly with increasing depth up to a maximum depth of 3 meters or up to

155 the bedrock border. In permafrost regions the mixing rates are much larger and vary based on soil conditions. It is assumed that cryoturbation is more effective in wetter soils and when the freezing during winter and the thawing during spring extends over a long periods – weeks to month – during which the soil repeatedly thaws and refreezes. To account for these effects, we assume a maximum diffusivity of 15 cm^2 year^{-1} which is scaled by two terms representing the (previous year's mean) saturation of the active layer and the number of days in which temperatures crossed the freezing point. At the surface, diffusivity D [cm^2

160 year^{-1}] is given by:

$$D(s) = 1.5 \qquad\qquad\qquad\qquad\qquad\qquad\qquad\qquad \text{; for bioturbation,} \qquad\qquad (3)$$

$$D(s) = 15 \cdot w_{atl} \cdot min\left(1, \frac{N_{dc0}}{N_{dc0,ref}}\right) \qquad\qquad\qquad \text{; for cryoturbation,} \qquad\qquad (4)$$

where w_{atl} is the saturation of the active layer, N_{dc0} the number of days per year in which surface temperatures crossed the freezing point and $N_{dc0,ref}$ a respective reference value which was set to 40 days year^{-1}. For the depth-dependency of

165 the mixing rates in permafrost-affected regions there are two options included in the scheme. Either a constant diffusivity is assumed throughout the active layer – or until the border with the bedrock –, or the mixing rates are assumed to decline linearly throughout the active layer.

The present model structure separates the organic matter into above and below ground pools and the vertical mixing de-

170 scribed above is only applied to the below ground carbon. The organic matter that is deposited above the surface needs to be incorporated into the soil before it can be transported into the deeper layers. The separation between above and below ground litter is a mere conceptual one – used to account for the different properties of the organic matter – and the above ground litter occupies the same physical space as the below ground pools representing the top soil layer. Hence, the transfer of carbon from the above to the below ground pools requires a change in properties rather than in space, and there are two ways by which this

175 can happen. The decomposition at the surface turns a given fraction of the organic matter into humus and with this transformation we assume a change in physical properties, that transfers the carbon from the above to the below ground pools (hence there is no above ground humus pool). Furthermore, organic matter builds up at the surface in grid boxes in which the long term carbon input at the surface is larger than the respiration rates. Here, we assume the load of organic matter at the surface to affect its properties, as the latter are largely dependant upon the material's bulk density which is reduced under pressure.

180 Thus, when the load of organic matter exceeds a given threshold – for the present study we choose ≈ 10 kg m^{-2} –, the excess material is transferred to the corresponding below ground pools. This corresponds to a surface organic layer with a maximum depth of around 15 cm –averaged over the grid box area–, when assuming a litter density of ≈ 75 kg m^{-3}, which is well within the range of typical organic layer thickness's (Yi et al., 2009; Lawrence et al., 2008; Johnstone et al., 2010) and very similar to the soil organic layer used in the study of Ekici et al. (2014).

Decomposition

With respect to the decomposition rates, k_{lc}, we follow the same approach as the standard YASSO model in which a lability-class-specific mass loss parameter, α_{lc}, is multiplied by factors accounting for the temperature and moisture dependencies of decomposition – d_{temp} and d_{mois}:

$$k_{lc} = \alpha_{lc} \cdot d_{temp} \cdot d_{mois} \tag{5}$$

For the above ground carbon pools we use the parametrizations of the standard model:

$$d_{temp}(s) = \exp(\beta_1 \cdot T_{surf} + \beta_2 \cdot T_{surf}^2) \qquad ; \text{with } \beta_1 = 0.095 \text{ and } \beta_2 = -0.0014, \tag{6}$$
$$d_{mois}(s) = 1 - \exp(\gamma \cdot P) \qquad ; \text{with } \gamma = -1.21, \tag{7}$$

where T_{surf} is the surface temperature [°C] and P the precipitation rate [$m\ year^{-1}$]. To account for the different decomposition rates under aerob and anaerob conditions we calculate the moisture dependency in inundated areas as (Kleinen et al., 2019):

$$d_{mois,inu}(s) = d_{mois}(s) \cdot 0.35 \tag{8}$$

It should be noted that we assume that only a fraction of the above ground organic matter in inundated areas decomposes under anaerob conditions. As discussed above, the above ground carbon pools in the model occupy the same physical space as the below ground pools representing the top layer of the soil column. In reality, however the litter that falls on top of a fully saturated soil column would still decompose aerobically unless there is standing water on top of the surface. Even then it is highly uncertain how much of the litter decomposes under anaerob or aerob conditions as this depends very much on it's shape and on the depth of the standing water – a twisted branch may be located largely above the water while a straight branch would be fully submerged. In the model we deal with this uncertainty be including the fraction of the above ground organic matter that decomposes anaerobically as an input parameter that can be varied between simulations (see below).

For the below ground decomposition rates, we evaluated a variety of functions to represent the moisture and temperature dependencies (Sierra et al., 2015), some of which are included as options in the present version of JSBACH. The goal of this evaluation was to establish a combination of dependencies that changes the carbon dynamics in the non-permafrost-affected regions as little as possible, while preserving the organic matter stored within the perennially frozen ground. For this study, we chose the temperature dependency parametrization of the YASSO model in combination with a simplified version of the moisture limitation function used in the CENTURY ecosystem model (Kelly et al., 2000). The temperature and moisture

dependencies, $d_{temp}(z)$, $d_{mois}(z)$ and $d_{mois,inu}(z)$ in depth z ($z \neq s$) are given by:

$$d_{temp}(z \neq s) = \exp(\beta_1 \cdot T_z + \beta_2 \cdot T_z^2), \tag{9}$$

$$d_{mois}(z \neq s) = 1.2 \cdot \left(\frac{w_z^* - b}{a - b}\right)^{d \cdot \frac{b-a}{a}} \cdot \left(\frac{w_z^*}{a}\right)^d \qquad \text{; with } a = 0.575, b = 1.5 \text{ and } d = 3, \tag{10}$$

215 $$d_{mois,inu}(z \neq s) = 1.2 \cdot \left(\frac{1 - b}{a - b}\right)^{d \cdot \frac{b-a}{a}} \cdot \left(\frac{1}{a}\right)^d \qquad \text{; for } w_{liq,z} > w_{ice,z}, \tag{11}$$

where T_z is the temperature in depth z and w_z^* represents the relative saturation of the soil, considering only the liquid water content. Note however, that we do not use the saturation of the soil directly, because certain formulations in the model's soil hydrology module prevent the soil moisture from dropping below a certain threshold or to increase beyond the soil's field capacity. In order to account for this, w_z^* is not given relative to the soils pore space, but relative to the range between the

220 wilting point and the field capacity. Additionally, we apply a subgrid scale distribution of the soil water in order to determine the inundated grid box fraction (see below). Thus w_z^* does not correspond to mean saturation of the grid box but to the saturation of the non-inundated fraction. In the inundated fraction soils are fully saturated and $d_{mois,inu}(z \neq s)$ has a fixed value of 0.32, it is assumed however that decomposition in the inundated areas can only occur when the liquid water content in a soil layer ($w_{liq,z}$) is larger than the layer's ice content ($w_{ice,z}$), even though it should be noted that in reality microbes do not necessarily

225 require free water in the soil to survive and they can maintain viability for thousands of years within frozen soils (Gilichinsky et al., 2003). However, we assumed the activity under these conditions to be negligible.

2.1.2 Permafrost-physics

The representation of the physical, permafrost-related processes in the soil are largely based on the implementation of Ekici et al. (2014). However, there are certain important differences, which will be described in more detail in the following. Most

230 importantly, we adapted the approach to representing soil organic matter from a pervasive organic-top-soil-layer to explicitly simulating the organic matter at the surface and within each of the vertical soil layers. Furthermore, we adapted the formulations of transpiration and the water limitations of plants to account for perennially frozen soils. It should be noted that the model accounts for the heat generated by decomposition (Khvorostyanov et al., 2008b), even though the effects are negligible in all the simulations.

235 Soil properties

The present model version represents the organic matter at and below the surface explicitly and accounts for respective effects on a given soil property, $X_{soil}(z)$, by aggregating the respective properties of organic, $X_{org}(z)$, and mineral material, X_{min}, according to their volumetric fractions, $f_{org}(z)$ and $(1 - f_{org}(z))$:

$$X_{soil}(z) = f_{org}(z) \cdot X_{org}(z) + (1 - f_{org}(z)) \cdot X_{min}. \tag{12}$$

The fraction of organic matter, $f_{org}(z)$, is given by:

$$f_{org}(z) = \frac{\rho_c(z)/r_{c2b}}{\rho_{org}(z)}, \tag{13}$$

where $\rho_c(z)$ is the mass concentration of carbon at depth z, r_{c2b} the carbon to biomass ratio and $\rho_{org}(z)$ the dry bulk density of organic matter. The estimates of $\rho_{org}(z)$ vary strongly depending on the quality of organic matter and whether it pertains to litter at the surface or to organic matter that is integrated in the soil (O'Donnell et al., 2009; Ahn et al., 2009; Chojnacky et al., 2009). For the present study, we chose $\rho_{org}(s) = 75$ kg m^{-3} for above ground organic matter and $\rho_{org}(z \neq s) = 150$ kg m^{-3} for the organic matter below ground. Likewise the properties of the organic matter, $X_{org}(z)$, differ between above and below ground organic matter (Peters-Lidard et al., 1998; Beringer et al., 2001; O'Donnell et al., 2009; Ahn et al., 2009; Chojnacky et al., 2009; Ekici et al., 2014). r_{c2b} was set to 0.5.

This aggregation was applied to all soil properties with the exception of the saturated hydraulic conductivity, for which we follow the approach of the Community Land Model (Oleson et al., 2013). Here, it is assumed that connected flow pathways form, once the fraction of organic matter exceeds a certain threshold. These need to be accounted for in the bulk hydraulic conductivity, $k_{sat}(z)$:

$$k_{sat}(z) = f_{uncon}(z) \cdot k_{sat,uncon}(z) + (1 - f_{uncon}(z)) \cdot k_{sat,org}(z) \tag{14}$$

where $f_{uncon}(z)$ is the grid box fraction in which no conected pathways exist, $k_{sat,uncon}(z)$ the saturated hydraulic conductivity in this fraction and $k_{sat,org}(z)$ the conductivity in the grid box fraction in which pathways form.

$$k_{sat,uncon}(z) = f_{uncon}(z) \cdot \left(\frac{1 - f_{org}(z)}{k_{sat,min}} + \frac{f_{org}(z) - f_{perc}(z)}{k_{sat,org}(z)} \right)^{-1} \quad ; \text{ with} \tag{15}$$

$$f_{uncon}(z) = 1 - f_{perc(z)} \quad ; \text{ and} \tag{16}$$

$$f_{perc}(z) = (1 - f_{thresh})^{-\beta_{perc}} \cdot (f_{org}(z) - f_{thresh})^{\beta_{perc}} \quad ; \text{ for } f_{org}(z) \geq f_{thresh}, \text{ and} \tag{17}$$

$$f_{perc}(z) = 0 \quad ; \text{ for } f_{org}(z) < f_{thresh}, \tag{18}$$

where $\beta_{perc} = 0.139$ and $f_{thresh} = 0.5$.

Soil and surface hydrology

A given fraction of the water within the soil remains liquid even at sub-zero temperatures. In reality, supercooled water exists in the presence of certain chemicals, such as salts, that lower the freezing temperature, but also because of the absorptive and capillary forces that soil particles exert on the surrounding water. The model does not represent the soil's chemical composition and we only account for the thin film of supercooled water that forms around the soil particles, which can be described by a freezing-point depression (Ekici et al., 2014; Niu and Yang, 2006). However, the liquid water is bound to the soil particles and it is questionable whether it is able to move through the surrounding soil-ice matrix. Thus, in the present model version, we assume the supercooled liquid water in the soil to be immobile. As the vertical movement of water requires flow pathways to

270 be available, percolation of liquid water within the soil is inhibited when more than half of the soil's pore space is occupied by
ice.

Additionally, the standard model version assumes lateral drainage from the soil at any given depth, which means that soil
ice in deeper layers has very little effect on the saturation of the soil column above. In the present model version, we allow
275 drainage only at the bedrock border, which results in permafrost acting as an effective barrier that strongly impedes drainage.
Finally, we changed the conditions controlling infiltration at the surface. In the standard model, infiltration is partly temperature
dependant, with no infiltration at the melting point. This condition was removed so that infiltration is controlled purely by the
saturation of the near-surface soil and the topography within the grid cell.

280 In JSBACH, transpiration and the plant's water stress are calculated based on the degree of saturation within the rootzone.
However, the respective parametrizations become very problematic in the presence of soil ice because they use a fixed parameter
– the maximum rootzone soil moisture – relative to which the degree of saturation is calculated. In reality, the rootzone in
permafrost-affected regions is confined to depths above the perennially frozen regions of the soil, while in the standard model,
the rootzone can not adapt to the permafrost table. Thus, the model's parametrization can result in plants experiencing constant
285 water stress when the permafrost extends into the rootzone, even if there is sufficient liquid water available in the upper layers.
Similarly, bare soil evaporation is determined by the saturation of the top 6.5 cm of the soil – considering only the liquid water
content relative to the entire pore space not to the ice-free pore space. Consequently, evaporation can be reduced substantially
when there is ice in the top soil layer, despite enough liquid water being present at the surface. In the present model version we
deal with this issue by accounting for the presence of ice and computing the saturation of the rootzone and the top soil layer
290 relative to the ice-free pore space.

2.1.3 Wetlands and inundated areas

In its standard version, JSBACH accounts neither for surface water bodies nor inundated areas and, for the present study, we
implemented two schemes that represent different aspects of their formation. Note that in the result section we make no differ-
entiation between wetlands and inundated areas because they have a very similar effect on the carbon cycle, in that they both
295 constitute areas in which soil organic matter decomposes under anaerobic conditions. The first scheme simulates the effect of
ponding – the formation of wetlands because water can not infiltrate fast enough and pools at the surface, while the second
scheme accounts for inundated areas that form in highly saturated soils, due to low drainage fluxes.

The ARNO model, which is used by JSBACH to determine the infiltration rates, does not account for ponding effects, instead
300 all water arriving on the soil surface is either infiltrated or converted into surface runoff (Dümenil and Todini, 1992; Todini,
1996). In the present version of JSBACH, we implemented a WEtland Extent Dynamics (WEED) scheme based on a concept
developed for the global hydrology model MPI-HM (Stacke and Hagemann, 2012). WEED adds a water storage to the land
surface which intercepts rainfall and snow melt prior to soil infiltration and runoff generation. Based on the storage's surface

area fraction f_{pond} and depth h_{pond}, evaporation E_{pond} and outflow R_{pond} are computed as

$$E_{pond} = (1 - f_{snow}) \cdot (f_{pond} - f_{skin}) \cdot E_{pot} \tag{19}$$

$$R_{pond} = h_{pond} \cdot \frac{1}{(1 - f_{pond}) \cdot \lambda_{pond}} \tag{20}$$

Outflow accounts for topography in form of the outflow lag λ_{pond} computed based on the orographic standard deviation σ_{oro}:

$$\lambda_{pond} = \left(1 - \left(\frac{\sigma_{oro}}{\sigma_{max}}\right)^{\frac{1}{4}}\right) \cdot \lambda_{max} \tag{21}$$

resulting in an increased outflow when either the storage contains a large amount of water or the orographic variability in the grid cell is high. Runoff is subdivided into direct infiltration and lateral runoff. The former is diagnosed as the soil moisture saturation deficit of the uppermost soil layer for the wetland covered grid cell fraction and directly added to the soil moisture storage. The latter is further processed into surface runoff and soil infiltration according to the standard soil scheme (Hagemann and Stacke, 2015; Dümenil and Todini, 1992). Runoff is assumed to be zero when temperatures fall below the freezing point. Considering all these fluxes, the water storage S_{pond} changes according to:

$$\Delta S_{pond} = P_{rain} + P_{melt} - E_{pond} - R_{pond} \tag{22}$$

Due to the coarse model resolution it is not reasonable to quantify f_{pond} for a given storage state explicitly from high-resolved topographical data. Instead, we attribute any change in the wetland's water volume $V_{pond} = S_{pond} \cdot f_{pond} \cdot A_{cell}$ to changes in the wetlands depth and extent using the topographical standard deviation of the grid cell:

$$\Delta h_{pond} = \left(\Delta V_{pond} \cdot \frac{\sigma_{oro}}{\sigma_{crit}}\right)^{\frac{1}{3}} \tag{23}$$

$$\Delta A_{pond} = \frac{V_{pond}}{h_{pond} + \Delta h_{pond}} - A_{pond} \tag{24}$$

Thus, any change in surface water is divided equally between water depth and extent if the orographic standard deviation of the grid cell equal a given critical orography standard deviation σ_{crit}. Thus, cells with a high orographic variation exhibit rather deep but small inundated fractions, while flat cells result in very shallow but extensive inundated fractions with a strong seasonality.

The WEED scheme is able to represent a realistic wetland distribution with extensive wetlands in the high northern latitudes and tropical rainforest regions. An extensive evaluation of the simulated water bodies is beyond the scope of the current study, but will be presented in an upcoming publication (Stacke et al, in preparation).

To determine the extent of inundation areas dynamically, we use an approach based on the TOPMODEL hydrological framework (Beven and Kirkby, 1979). TOPMODEL employs sub-gridscale topographic information contained in the compound topographic index (CTI) to redistribute the grid-cell mean water table, raising the sub-grid-scale water table in areas of high CTI and lowering it where CTI is low. We employ the CTI index product by Marthews et al. (2015) for the CTI index

at a resolution of 15 arcseconds to determine the distribution of CTI values within any particular grid cell and thus determine
335 the fraction of the grid cell where the water tale is at or above the surface. A detailed description of the approach is given by
Kleinen et al. (2019).

2.1.4 Gases in the soil

The standard version of JSBACH does not differentiate between aerobic and anaerobic soil respiration and, to be able to
340 determine the methane emissions from saturated soils, we implemented the methane model proposed by Kleinen et al. (2019).
Based on Riley et al. (2011), the model determines CO_2 and CH_4 production in the soil, the transport of CO_2, CH_4 and O_2
through the three pathways diffusion, ebullition and plant aerenchyma, as well as the oxidation of methane whereever sufficient
oxygen is present. Partitioning of the anaerobic decomposition product into CO2 and CH4 is temperature-dependent, with a
baseline fraction of CH_4 production $f_{CH4} = 0.35$ and a Q10 factor for f_{CH4} of Q10 = 1.8 – with a reference temperature of
345 295K. In each grid cell the methane model determines CH_4 production and transport for two grid cell fractions, the aerobic
(non-inundated) and the anaerobic (inundated) fraction of the grid cell. If the inundated fraction changes, the amounts of CO_2,
CH_4 and O_2 are conserved, transferring gases from the shrinking fraction to the growing fraction, proportional to the area
change. Thus the model captures not just the emission of methane from inundated areas, but also the uptake and oxidation of
methane by the soil in the non-inundated areas.

2.2 Experimental setup

2.2.1 Simulations

The modifications described above change the model's behaviour substantially, which introduces large, additional uncertain-
ties. These involve uncertainties that originate from the parametrizations themselves but also from their interactions with other
processes in the model. To account for these uncertainties we created an ensemble of 40 simulations in which key parameter
355 values and parametrizations were varied (see below). However, the ensemble-size, in combination with the temporal extent of
the simulations, made it infeasible to use the fully coupled MPI-ESM which has roughly a hundred times the computational
demand of the land surface model. Instead we use JSBACH in an offline-setup, in which the land surface model is driven by
output from the fully coupled model. Here, we use output from simulations with the standard version of the MPI-ESM1.2 that
were performed in the context of the 6th phase of the Coupled Model Intercomparison Project (CMIP6) (Eyring et al., 2016).
360 These simulations cover the historical period – 1850 to 2015 – and a scenario period ranging between the years 2016 and 2100.

The present study aims to investigate the high latitude's response to increasing and decreasing atmospheric green-house gas
concentrations and, because it is often easier to understand the underlying mechanisms when the effects are large, we inves-
tigate a high GHG emission trajectory based on the Shared Socioeconomic Pathway 5 and the Representative Concentration
365 Pathway 8.5 (SSP5-RCP8.5), even though this is not necessarily the most likely scenario (van Vuuren et al., 2011; Riahi et al.,

2017). SSP5-RCP8.5 targets a radiative forcing of 8.5 W m^{-2} in the year 2100 and assumes the atmospheric CO_2 concentrations to increase to about 900 ppmv by the end of this century, while the global mean temperature rises to about 4 K above pre-industrial levels and the precipitation rates in the high northern latitudes to about 675 mm year^{-1} (Fig. 1). There are no scenario simulations available that could provide the forcing for a decrease in GHG concentrations and, for the present study,

370   we assume that the decrease simply reverses the trajectory of the increase prior to the peak. Here, we simulate the response to decreasing GHG concentrations after peaks in the years 2025, 2050, 2075 and 2100.

All simulations have the same general setup, with a horizontal resolution of T63 (1.9° × 1.9°), which corresponds to a grid-spacing of about 200 km in tropical latitudes, a temporal resolution of 1800 seconds and a vertical resolution of 18 sub-surface

375   layers that reach to a depth of 100 m, 11 of which are used to represent the top 3 meters of the soil column (Note that for the present study, we chose the vertical resolution within the top of the soil column fine enough to be able to run both the soil physics and the vertical carbon transport on the same vertical layers). Each simulation is initialized in the year 1850 and the first 150 years of a simulation are used as a spin-up period. As stated above, the modifications of the model introduce additional uncertainty and our strategy was not to choose the best estimate for the many of the parameters, but rather vary them within

380   the plausible range to capture the uncertainties that are involved in the respective parametrisations.

One key factor, determining the processes in the high latitudes, is the treatment of the soil properties, especially the treatment of the organic matter at and below the surface (Lawrence et al., 2008; Ekici et al., 2015; Jafarov and Schaefer, 2016; Zhu et al., 2019). For the study we chose 5 different configurations, which result in substantially different soil thermal and

385   hydrological properties and, consequently, substantial differences in the simulated sub-surface dynamics (Fig. 2 a-c). In 3 of these configurations we use the entirety of adaptations described above and merely vary the properties assumed for the soil organic matter (Note that in one configuration we also prevented the infiltration at sub-zero temperatures and allowed the movement of supercooled water in the soil to be as close to the standard model as possible). The other two configurations are much more similar to the approach used by Ekici et al. (2014). In the approach, the organic matter only has an impact on the

390   soil properties of the first soil layer, while the lower layers have the properties of mineral soil. The difference between these 2 configurations is the properties assumed for the organic matter. Another important factor is the nitrogen limitation in the model. The changes in the model's hydrology scheme increase the leaching of mineral nitrogen in the high latitudes, which reduces the nitrogen availability substantially. The corresponding nitrogen limitations are much higher than in the standard model which has a drastic impact on the simulated vegetation dynamics and decomposition rates (which are also limited by the nitrogen

395   availability). But rather than re-tune this highly uncertain parametrization we performed an additional set of simulations in which the nitrogen limitations were neglected, capturing the range between highly over- and underestimated nitrogen limitations (Fig. 2 d-f). Furthermore, a key parameter with respect to the methane emissions is the fraction of above-ground organic matter that decomposes anaerobically in the inundated fraction of the grid box. Here, we performed one set of simulations in which we choose a low value – 0.4 – and one set of simulations with a high value – 0.8 – for this parameter. Finally, we varied

400   key parameters in in the methane module, most importantly the maximum oxidation velocities, which resulted in two sets of

simulations which are largely identical but give very different CO_2 and CH_4 emissions. In total, this gives:

$$n_{sim} = n_{c,soil} \cdot n_{c,nitro} \cdot n_{c,decomp} \cdot n_{c,CH4}, \qquad (25)$$

where n_{sim} is the total number of simulations (40), $n_{c,soil}$ the number of configurations with respect to the soil properties (5), $n_{c,nitro}$ the number of configurations with respect to nitrogen limitations (2), $n_{c,decomp}$ the number of configurations with respect to the fraction of above-ground organic matter that decomposes anaerobically in the inundated fraction (2) and $n_{c,CH4}$ the number of configurations with respect treatment of gases in the soil (2).

2.2.2 Initial carbon pools

Determining the initial soil carbon concentrations is very challenging especially for the northern high latitudes where organic matter was stored in the frozen soils under the cold climate during and since the last glacial period (Zimov et al., 2006; Zimov, 2006b; Schuur et al., 2008). Simulations that target the build up of the soil carbon pools in permafrost-affected regions need to cover the carbon dynamics over a similar period (von Deimling et al., 2018). The respective simulations require many simplified assumptions and, because of the extensive timescale, even small uncertainties propagate into substantial differences between simulated and observed carbon pools. Another strategy is to initialize the simulations with observed soil carbon concentrations (Jafarov and Schaefer, 2016). These rely on the spatial extrapolations of thousands of soil profiles (Batjes, 2009, 2016; Hugelius et al., 2013) and can be considered much closer to reality than any modelling effort that we are aware of. However, this approach has the disadvantage that the carbon pools are not necessarily consistent with the simulated climate, which can result in unrealistic carbon fluxes at the beginning of a simulation. Furthermore, there is only little information on the quality of the soil organic matter, making it very difficult to separate the carbon into the lability classes used by the model. Here, we choose a combination of the two approaches to achieve some consistency with both, observed soil carbon pools and the simulated climate.

To initialize the soil carbon concentrations, we use the vertically resolved, harmonized soil property values provided by the WISE project (Batjes, 2009, 2016). While the dataset only covers the top 2 meters of the soil column – other datasets provide information up to a depth of 3 meters (Hugelius et al., 2013) – it has the important advantage that it is consistent with the FAO soil units which were used to derive the soil properties for the JSBACH model (Hagemann et al., 2009; Hagemann and Stacke, 2015). The dataset provides no information on the quality of the organic matter and we distribute the soil carbon among the lability classes according to the pre-industrial equilibrium distribution that is simulated with the MPI-ESM. However, we do not assume the same distribution in all soil layers and make additional assumptions for different lability classes. The highly labile organic matter has a mass loss parameter that corresponds to a reference decomposition time ranging from a few days to a few years and the respective organic matter decomposes before it can be mixed throughout the soil column. Thus we assume that its vertical profile resembles that of the carbon inputs and distribute the highly labile carbon according to an idealized root profile. In contrast the humus pool has a reference decomposition time of several hundred years, allowing it to be well mixed

throughout the soil, and we assume a similar humus concentration in all layers.

$$C_{fast}(l) = TC_{obs} \cdot f_{fast,sim} \cdot y(l) \cdot dz(l)^{-1} \qquad\qquad , \text{ with } TC_{obs} = \sum_{i=1}^{nlayers} C_{obs}(i) \cdot dz(i), \qquad (26)$$

435 $$C_{slow}(l) = C_{obs}(l) \cdot f_{slow,sim}, \qquad\qquad (27)$$

where $C_{fast}(l)$ is the concentration of highly labile carbon in layer l and $C_{slow}(l)$ the humus concentration. $f_{fast,sim}$ and $f_{slow,sim}$ are the respective shares in the total soil carbon as simulated with the MPI-ESM. $C_{obs}(l)$ is the observed carbon concentration in layer l, TC_{obs} the total amount of carbon in a given grid box, $y(l)$ the root-fraction and $dz(l)$ the thickness of layer l.

440

In a first step we calculate C_{fast} with the above formula but apply the condition that wherever $C_{fast}(l) > C_{obs}(l)$, the excess in carbon was shifted to the nearest layer in which $C_{fast}(l) < C_{obs}(l)$. In a second step we calculated C_{slow}, iteratively applying the condition that wherever $C_{slow}(l) > (C_{obs}(l) - C_{fast}(l))$ the excess was added to the nearest layer in which $C_{slow}(l) < (C_{obs}(l) - C_{fast}(l))$. After $C_{fast}(l)$ and $C_{slow}(l)$ have been determined, $C_{med}(l)$, the concentration of organic
445 matter with a decomposition timescale of tens of years, is calculated as the difference between $C_{obs}(l)$, and the sum of $C_{fast}(l)$ and $C_{slow}(l)$:

$$C_{med}(l) = C_{obs}(l) - (C_{fast}(l) + C_{slow}(l)). \qquad\qquad (28)$$

To minimize the inconsistency between observed carbon concentrations and simulated climate conditions, we initialize the experiments with the observation-based, present-day carbon pools but start the simulations in the year 1850 at the end of the
450 pre-industrial period. In the high northern latitudes this allows the carbon concentrations within the (simulated) active layer to adapt to the simulated climate conditions during the historical period, while the perennially frozen regions of the soil conserve the observed carbon concentrations. As the soil thermal and hydrological dynamics vary depending the treatment of the soil properties, this initialisation approach results in substantially different soil carbon pools at the end of the spin-up period.

3 Results

455 At the beginning of the 21st century, regions that are affected by near-surface permafrost, here defined as featuring perennially frozen soils within the top 3 meters of the soil column (Andresen et al., 2019), contain roughly between 800 and 1400 Gt of carbon (Fig. 2 a, Tab. 1). 375 to 620 Gt(C) of these are located within the active layer, where they are exposed to microbial decomposition, and the resulting soil CO_2 emissions range between roughly 3.0 and 4.5 Gt(C) year^{-1}. In most simulations, these emissions are not fully balanced by the soil's carbon uptake, resulting in net fluxes of between -0.1 and 0.6 Gt(C) year^{-1}
460 meaning that, most likely, the high-latitude soils no longer act as a carbon sink at the beginning of the 21st century. This is also the case for the terrestrial ecosystem as a whole, that is when also accounting for changes in vegetation biomass (Fig. 3 a). Almost all simulations estimate the ecosystem's carbon flux into the atmosphere to be positive at the beginning of the

21st century – on average around 0.1 Gt(C) – and none of the simulations predicts the transition from carbon sink to source to occur after the year 2023. The net carbon emissions increase substantially with rising GHG concentrations, and even for the

465 temperature target of the Paris Agreement – global mean surface temperatures about 1.5 K above pre-industrial levels – the simulated net fluxes increase by a factor of 5 - 6, while for a temperature rise of 2.5 K the net emissions would be over 10 times larger than at the beginning of the century. Here, the ecosystem emissions exhibit a non-linear and strongly hysteretic dependency on the simulated surface temperatures and the fluxes into the atmosphere are substantially lower after than before the GHG peaks in 2050, 2075 and 2100. The ecosystem's net carbon flux is largely determined by CO_2 exchange between the land

470 – soil and vegetation – and the atmosphere, while methane emissions contribute very little to the overall carbon flux (Fig. 3 b,c).

3.1 Soil CO_2 flux and carbon uptake

The CO_2 emissions from permafrost-affected soils are very sensitive to changes in the atmospheric GHG concentration making a substantial increase in soil CO_2 fluxes very likely, should 21st-century GHG emissions follow the SSP5-RCP8.5 scenario.

475 The fluxes depend on a number of factors that are affected by the atmospheric GHG concentrations, most importantly the changing climate conditions. As a result, the soil emissions exhibit a non-linear dependency on the atmospheric CO_2 concentrations (not shown) but an almost linear dependency on the simulated surface temperatures (Fig. 3 b) – where, very roughly, each degree of warming increases the soil CO_2 fluxes by 50%, relative to the emissions at the beginning of the century. For the temperature target of the Paris Agreement, the soil emissions increase by about 25% to 40% and if GHG concentrations follow

480 SSP5-RCP8.5 until the year 2100, the soil CO_2 fluxes potentially increase by over 150%, resulting in fluxes of roughly 6.5 to 13.5 Gt(C) year^{-1}. The (almost) linear temperature dependency of the soil CO_2 fluxes is also valid for decreasing temperatures and, when the GHG forcing is reversed, the soil CO_2 fluxes decrease on a trajectory very similar to the increase prior to the GHG peak. However, this does not necessarily mean that the main processes governing the changes in soil CO_2 emissions are fully reversible on a decadal to centennial timescale (see below).

485

One reason for the strong increase in soil CO_2 fluxes with rising temperatures is the degradation of near-surface permafrost and the corresponding increase in active layer depth. For a GHG peak in 2100 over 80% of the near-surface permafrost disappear (Fig. 4 a), exposing large amounts of organic matter to conditions which allow for microbial decomposition. The rise in soil respiration, resulting from the increased exposure of formerly frozen carbon, reduces the soil organic matter substantially

490 and for a GHG peak in 2100 the total amount of carbon stored in permafrost-affected soils could be reduced by close to 15% (Fig. 4 b). This corresponds to a loss of roughly 150 ± 50 Gt(C), which is at the higher end of previous estimates (Schuur et al., 2013; Schaefer et al., 2014). Because the soils remain net carbon emitters even after the GHG forcing is reversed, the soil carbon pools continue to decline after the GHG peak, resulting in a carbon loss of up to 20%. When temperatures have returned to the level of the beginning of the century the overall loss in soil carbon amounts to 120 - 240 Gt(C), a large fraction

495 of which is irreversible – at least on short timescales – because it pertains to carbon stored within the frozen soils.

Even though these soil carbon losses are substantial, the increased exposure of organic matter stored in permafrost soils is insufficient to explain the rise in soil CO_2 fluxes, given that the relative increase in the fluxes is a lot larger than the increase in active layer carbon (Fig. 4 c, d). Furthermore, the largest fraction of the recently exposed carbon takes a long time to de-
500 compose (Fig. 4 c), while the relative increase in readily decomposable material within the active layer is much smaller (Fig. 4 d). Here, the amount of labile active layer carbon starts to decrease even before the GHG peak in 2100 is reached, while the soil CO_2 fluxes continue to increase. Furthermore, the labile carbon in the active layer shows a strongly hysteretic behaviour and after the GHG peak there is substantially less labile organic matter in the active layer than prior to the GHG peak, while there is slightly more stable organic matter. This indicates that, in addition to the overall carbon loss, the permafrost affect soils
505 undergo major compositional changes which should lead to a reduction of the soil CO_2 fluxes.

Another important driver of the soil CO_2 fluxes is the carbon input into the soil, which is largely dependant upon the vegetation's net primary productivity (NPP). The NPP, in turn, depends on the atmospheric GHG concentrations directly, as this determines the CO_2 uptake by leaves, and indirectly, through the resulting climate conditions – namely surface temperatures
510 and water availability – and the vegetation distribution – characterised by the type of vegetation and the vegetation cover. Overall, the changes in climate conditions make the high latitudes much more habitable for plants. The surface temperatures in the Arctic increase about twice as fast as global mean temperatures (Fig. 5 a). This does not only extend the growing season but also increases the water availability for plants, because higher soil temperatures cause the soil ice to melt earlier and refreeze later during the year. Together with the increase in precipitation (Fig. 1 d), this raises the plant-available water by as much as
515 55% (Fig. 5 b). The changes in climate conditions also increase the vegetation cover and facilitate a (relative) shift from grasses and shrubs towards more productive trees (Fig. 5 c). In combination with the direct effect of CO_2 fertilization, the changes in climate and vegetation increase the NPP in permafrost-affected regions substantially, roughly doubling the productivity for the GHG peak in 2100 (Fig. 5 d).

520 This increase in NPP corresponds to an increase in carbon input into the soil of up to 4 Gt(C) year^{-1} and, while GHG concentrations increase, about half of the increase in soil CO_2 emissions is balanced by the increase in primary productivity. After the GHG peak, the NPP is consistently larger than before the peak, mostly because the tree cover remains very high, resulting in substantially larger carbon inputs than prior to the peak. This balances the reduced amount of labile carbon in the active layer, explaining why soil CO_2 emissions can even be larger when temperatures have returned to the levels of the
525 beginning of the century despite there being up to 30% less labile carbon and about 20% less highly labile carbon in the active layer (Tab. 1). Thus, the predominant absence of hysteresis in the simulated soil CO_2 emissions does not mean that the governing processes are fully reversible on short timescales, but that it is the result of two strongly hysteretic factors offsetting each other – before the GHG peak the large CO_2 fluxes are supported by the deepening of the active layer, while it is largely the increase in NPP that drives the post-peak CO_2 fluxes. The larger carbon uptake by plants following the GHG peak also
530 explains the hysteresis of the ecosystem's net carbon flux – with similar soil CO_2 fluxes and a substantially larger NPP the flux into the atmosphere is consistently smaller after than prior to the GHG peak.

3.2 CH$_4$

The methane emissions from permafrost-affected soils behave very differently than the soil CO$_2$ fluxes. Most importantly, the soils' CH$_4$ emissions are 3 orders of magnitude smaller than the respective CO$_2$ fluxes, indicating that methane will play only

535   a minor role in the northern high latitudes' contribution to global warming, even when considering the respective difference in global warming potential. At the beginning of the 21st century the simulated net CH$_4$ emissions from high latitude soils amount to roughly 9 Mt(C) year^{-1} – or about 9 Tg(CH$_4$) year^{-1}. With a global warming potential of 28 times that of CO$_2$ (Stocker et al., 2013), this corresponds to a CO$_2$ flux of 0.25 Gt(C) year^{-1}. Here it should be noted that the spread in the simulated methane fluxes is substantial, but even the largest net CH$_4$ emission of any of the simulations is around 34 Mt(C)

540   year^{-1}, which has the warming potential of a CO$_2$ flux of 0.9 Gt(C) year^{-1}.

One reason for the low soil CH$_4$ fluxes is the temperature dependency that determines the ratio of CH$_4$ and CO$_2$ which are being produced during the anaerobic decomposition of organic matter. For the low temperatures that are characteristic for the high northern latitudes, only a small fraction – on average around 10% – of the organic matter is converted into methane,

545   even though this rate can increase to 50% for more moderate temperatures. Furthermore, the area in which organic matter decomposes anaerobically is comparatively small. The vast majority of all inundated areas are only seasonally flooded so that anaerobic conditions in the soil exist only temporarily, predominantly during late spring and early summer (Fig. 2 g-i). Thus, while there are regions in western Siberia where up to 40% of the surface are inundated during the snow melt season, the average inundated fraction in permafrost-affected regions ranges roughly between 4% and 6%, which increases to about 10%

550   to 12% when only considering the period of April - June. On one hand this means that the amount of organic matter that is decomposed under anaerobic conditions is roughly an order of magnitude smaller than the amount decomposed under aerobic conditions – around 0.2 Gt(C) year^{-1} compared to 4 Gt(C) year^{-1}. On the other hand, it means that the largest fraction of the high-latitude soils produces no methane but actually takes up atmospheric CH$_4$, oxidising it to CO$_2$.

555   The way the CH$_4$ emissions react to the changes in atmospheric GHG concentrations also differs substantially from the CO$_2$ fluxes (Fig. 3 c). There is almost no increase with rising GHG levels and when global mean surface temperatures rise beyond 2.5 K above pre-industrial levels, the emissions even start to decrease. This is very different to the results of previous modelling studies, who found a strong, positive connection between the 21st century temperature rise and methane emissions (Khvorostyanov et al., 2008a; Burke et al., 2012; von Deimling et al., 2012; Schuur et al., 2013; Lawrence et al., 2015). In

560   large parts, the behaviour of the simulated methane emissions is a result of the dependency of the net CH$_4$ fluxes on the atmospheric methane concentrations, as the former are determined by the CH$_4$ gradient between the soil and the atmosphere. The SSP5-RCP8.5 scenario predicts the atmospheric methane concentrations to double by the end of the 21st century (Fig. 1 b). Consequently, the methane concentrations in the soil have to increase similarly merely to maintain constant CH$_4$ fluxes. The same is true for the CO$_2$ fluxes, however there is an important difference. When the soil-atmosphere-CO$_2$ gradient de-

565   creases due to increasing atmospheric GHG concentrations, CO$_2$ rapidly accumulates in the soil until an equilibrium with the

atmospheric concentrations is reached that allows to respire the CO_2 generated by decomposition. In contrast, it is much more difficult for the CH_4 concentrations to build up within the soils because a large fraction of the methane is constantly converted into CO_2 in the oxygen-rich layers near the surface. Additionally, larger atmospheric methane concentrations increase the CH_4 flux into non-saturated soils that do not produce methane. For atmospheric methane concentrations that correspond to

570   the temperature target of the Paris Agreement, this could potentially lead to the average CH_4 fluxes from permafrost-affected soils becoming negative. For larger atmospheric GHG concentrations, the high northern latitudes could continue to act as a net methane sink even while rising temperatures increase the CH_4 production within the soil.

However, the atmospheric CH_4 concentration can not explain why the methane fluxes are substantially smaller following

575   the GHG peak and why the high latitude soils may remain a methane sink when the forcing is fully reversed and atmospheric GHG concentrations have returned to present-day levels. The highly hysteretic behaviour of the methane emissions is the result of changes in the methane production in the soil and the way methane is transported towards the surface. The soil respiration depends on the availability of organic matter and the decomposition rates which are determined by the conditions under which the organic matter decomposes. These conditions are not only affected by changes in near-surface climate but also vary de-

580   pending on the organic matter's (vertical) position within the soil, making the soil CH_4 emissions strongly dependent upon changes in the vertical soil carbon profile.

The most important effect of rising GHG concentrations is an increase in soil and surface temperatures. While rising temperatures have a predominantly positive effect on the soil respiration, due to the temperature dependency of the decomposition

585   rates, they can be detrimental to the occurrence of inundated areas and saturated soils, hence the areas where organic matter is decomposed under anaerobic conditions. On one hand rising temperatures increase evapotranspiration in summer which decreases the inundated areas after the spring snow melt. On the other hand, ice within the deeper layers of the soil acts as a barrier and the soils drain much more readily when this barrier is melted. Rising GHG concentrations also increase precipitation rates by up to 25% (Fig. 1 d), partly balancing the negative effect that higher temperatures have on the extent of inundated

590   areas. The combined effect of increasing temperatures and precipitation rates is a slight drying of the soils, which has also been found by other models (Andresen et al., 2019). However, the drying of the soil has very little impact on the overall extent of inundated areas (Fig. 6 a). Rather than shrink, the spatial distribution of inundated areas adapts to the changes in climate conditions – with their extent decreasing in lower and increasing in higher latitudes (Fig. 7). Furthermore, the liquid soil water content in regions that feature large wetland areas increases substantially (Fig. 6 b), while the overall water content (including

595   soil ice) declines only slightly (not shown).

With a similar extent in the inundated area and increasing temperatures, the soil methane production mainly benefits from the changes in climate. However, the oxic soil respiration in the adjacent non-inundated areas increases even more because, in addition to the effects of rising temperatures, the increase in liquid water content reduces the moisture limitations on the oxic

600   decomposition rates. Furthermore, the vertical distribution of organic matter in the soil changes in a way that also increases the

CO_2 production relative to that of CH_4. The largest fraction of the carbon inputs occurs above or close to the surface. Thus the increase in NPP, resulting from rising GHG concentrations, primarily increases the carbon concentrations at the top of the soil column (Fig. 8 a, b). At the surface the oxic decomposition rates are much larger than those under anoxic conditions, while this difference is less pronounced deeper within the soil. Consequently, the (relative) increase in organic matter at the surface

605   further increases the difference between the oxic and anoxic respiration rates. When the forcing is reversed, the factors that determine the difference between the decomposition rates do not return to their state prior to the GHG peak – the distribution of inundated areas remains very different (Fig. 7), the liquid water content in the soil remains much higher (Fig. 6 b) and the soil carbon profile still exhibits higher concentrations of organic matter closer to the surface (Fig. 8 c). Consequently, the difference between oxic and anoxic decomposition rates are also larger after than prior to the GHG peak.

610

The difference in the decomposition rates is highly relevant for the soil methane production. The largest fraction of the anaerobic decomposition takes place in seasonally saturated soils, which means that, for a given period, the organic matter in the respective areas decomposes under aerobic conditions. Consequently, the soil methane production depends on both, the anoxic and the oxic decomposition rates, as the latter determine how much organic matter is decomposed during the drier

615   month, hence how much organic matter is available at the onset of inundation.

The inundated area is largest during spring and early summer – April to July – with a peak in May and June followed by a sharp decline due to a strong increase in evapotranspiration (Fig. 9 a). The productivity, on the other hand, peaks in July and the decomposition rates and the litter flux even later. Thus, a large fraction of the carbon input into the soils occurs when conditions

620   favour oxic over anoxic decomposition. Increasing temperatures strengthen this effect because the extent of inundated soils increases during spring – due to larger snow melt fluxes – while it decreases during summer, owing to higher evapotranspiration and drainage rates (Fig. 9 b). Most importantly, the increase in oxic decomposition rates is far larger than the increase in anoxic decomposition rates. Thus when GHG concentrations increase, the largest fraction of the additional organic matter – resulting from the increased productivity and the deepening of the active layer – is being respired under oxic conditions in summer and

625   fall when the extent of inundated areas is relatively small. Additionally, higher soil temperatures lead to a larger fraction of the fresh litter being decomposed aerobically during winter, resulting in a lower soil carbon availability during and after the following snow melt season. As a result the relative increase in oxic soil respiration in regions that feature large wetland areas is roughly twice as large as the relative increase in methane production (Fig. 6 c,d).

630   When the GHG forcing is reversed, there is less organic matter within the active layer, especially during summer and fall, but the decomposition rates and the litter flux remain higher than prior to the peak (Fig. 9 c). In case of the aerobic soil respiration, the increase in decomposition rates is so large that the soil respiration during winter and spring is actually larger than prior to the GHG peak, despite the reduced availability of organic matter. This partly balances the reduction in soil respiration during summer and fall and the annually averaged aerobic soil respiration following the GHG peak is only slightly smaller than prior

635   to the peak. In contrast, the anoxic decomposition rates increase just enough to balance the reduced soil carbon availability dur-

ing the winter and spring months, while there is substantially less anoxic soil respiration during summer and fall. In case of the anoxic respiration, the effect of the lower soil carbon availability is even more severe because more organic matter – including the litter input – has been respired aerobically during the previous dry period. Thus, because the anaerobic decomposition rates are much lower than the aerobic rates, while both anoxic and oxic respiration (partly) depend on the same carbon pools, the

640   relative changes in oxic and anoxic respiration are very different. In regions that feature large extents of inundated areas, the oxic respiration is only a few percent lower after than before the GHG peak, while the soil methane production is reduced by up to 30% (Fig. 6 c,d).

    Still, even the reduced methane production can not fully explain the difference in the net CH_4 emissions before and after

645   the GHG peak. Another important factor is the methane-transport in the soil and how this is affected by the changes in the vertical soil carbon profile. There are two major pathways by which methane is transported towards the surface, one being the diffusive transport through the soil, the other being plant-mediated transport (Note that the model also simulates ebulition, but the respective fluxes can be neglected). Even in saturated soils, the layers near the surface have a high oxygen content and the better part of the methane that diffuses upwards is oxidised within these layers. Consequently, the largest methane fluxes at the

650   surface do not result from vertical diffusion, but from the methane release by (vascular) plants, whose roots absorb methane within the soil. Here, the changes in the vertical soil carbon profile alter the fraction of methane that is transported towards the surface by a given transport mechanism. When the share of organic matter increases close to the surface and decreases in the deeper layers, a smaller fraction of the methane produced in the soil can be absorbed by roots, substantially reducing the respective emissions at the surface. In a addition there is a 5% decrease in cover fraction of grasses, which are the most

655   effective gas transporters (not shown). As a result, the methane emissions by plants decrease by up to 60% when the GHG forcing is fully reversed, which is a reduction roughly twice as large as the relative decrease in the soil methane production (Fig. 10 a). In contrast, the oxidation rates differ comparatively little before and after the GHG peak (Fig. 10 b), because the lower methane concentrations in the soil lead to a larger uptake of atmospheric CH_4. Thus, with a reduced methane production and a larger CH_4 uptake the soil's net emissions decrease substantially, potentially turning the permafrost-affected regions into

660   a net CH_4 sink.

4   Conclusion

One of the most important factors in the permafrost-carbon-climate feedback is the fraction of soil carbon that is released in the form of CH_4, which is tightly connected to the question of whether the high latitudes will become wetter or drier in the future (Schuur et al., 2015). Here, many land surface models indicate a drying of the high latitudes (Anderson, 2019) which will most

665   likely constrain the decomposition under anaerobic conditions (Oberbauer et al., 2007; Olefeldt et al., 2012; Elberling et al., 2013; Schaedel et al., 2016; Lawrence et al., 2015). In parts, this is confirmed by results of our study and while we did not find a decrease in the extent of areas with saturated soils, we also did not find a significant expansion of the inundated areas in high latitudes despite the pronounced increase in precipitation resulting from the SSP5-RCP8.5 scenario. Furthermore, we could

show that the high latitude methane fluxes are strongly limited by the increase in oxic decomposition because most of the soils
670 are only seasonally saturated and the availability of organic matter depends on the respiration during the drier month of the
year. But most importantly, we found the methane oxidation in the soil to be the dominant constraint on the soil CH_4 emissions.
Even for present conditions, only a quarter of the methane produced in permafrost-affected soils was actually emitted at the
surface. With the atmospheric CH_4 concentration increasing and the vertical methane transport by vascular plants decreasing,
this fraction could be reduced to less than 10 % in the future. Because of these limitations, there was not a single year –
675 from 20000 years of simulation (500 years for 40 ensemble members) – in which the methane emissions from permafrost-
affected soils exceeded 55 Mt(C) year^{-1}. Considering the global warming potential of methane, this corresponds to a CO_2 flux
of about 1.5 Gt(C) year^{-1}, which is an order of magnitude smaller than the largest simulated CO_2 flux – about 14 Gt(C) year^{-1}.

Thus, our results indicate that the soil methane fluxes in permafrost-affected regions do not constitute an important contribu-
680 tor to the climate-carbon feedback. In contrast, the soil CO_2 emissions are so large that the (terrestrial) arctic ecosystem acts as
a source for atmospheric CO_2, with net emissions of up to 0.4 Gt(C) year^{-1} at the beginning and up to 3.9 Gt(C) year^{-1} at the
end of the 21st century. This is very different to scenario simulations with the standard version of the MPI-ESM1.2 in which
the region continues to take up atmospheric CO_2 throughout the entire 21st century, with the uptake increasing from around
0.005 to around 0.015 Gt(C) year^{-1} (not shown). These differences confirm that the non-consideration of permafrost-related
685 processes and the organic matter stored in the frozen soils leads to a fundamental misrepresentation of the carbon dynamics in
the Arctic.

Here, the differences in simulated net emissions in the high northern latitudes – between the standard and the modified JS-
BACH version – are so large that they become highly relevant for the global carbon budget. For the present-day (2007 - 2016)
690 the terrestrial carbon sink has been estimated to about 3 Gt(C) year^{-1} (Quéré et al., 2018) and net emissions from permafrost-
affected soils of 0.4 Gt(C) year^{-1} would reduce the land's capacity to take up carbon by more than 10%. It should be noted
that the net emissions of 0.4 Gt(C) year^{-1} may even be a conservative estimate as our study considered only regions that still
featured near-surface permafrost in the year 2000, while the area in which the high latitude soils act as a source of atmospheric
CO_2 was substantially larger. With the advancing degradation of near-surface permafrost, the respective CO_2 fluxes will be-
695 come even more important for future carbon budgets and already by 2050 the net emissions from permafrost-affected soils
could be on par with (present-day) global land use change emissions.

Despite their importance, the processes governing the carbon dynamics in permafrost-affected regions are not fully taken into
account in the present generation of Earth-system models. Substantial advances have been made within the last decade – many
700 land surface models now include some physical and biogeochemical permafrost processes (McGuire et al., 2016; Chadburn
et al., 2017) –, but not one of the models that participated in CMIP6 included an adequate representation of the soil physics
in high latitudes, while simulating (interactive) vegetation dynamics as well as the carbon and nitrogen cycle. Consequently,
model based studies, at present, can merely provide qualitative answers to the question how permafrost-thaw may contribute

to global warming (Schuur et al., 2015). Even when the most relevant processes are included, there are large uncertainties
705 regarding the respective parametrizations as well as the initial- and boundary conditions used by the model – many of which
are only poorly constrained by observations. In the present study we used an ensemble of simulations in which we varied key
parameters within the uncertainty range and while the simulations agreed on the system's relative response to increasing and
decreasing GHG concentrations, the spread in the absolute values was substantial between the ensemble members, e.g. the
simulated carbon pools at the beginning of the 21st century ranged between 800 and 1400 Gt while the soil methane emissions
710 ranged between 0.5 and 34 Mt(C) year^{-1}. To be able quantify the impact of permafrost degradation on the climate system,
these uncertainties need to be reduced substantially.

Code and data availability. The primary data is available via the German Climate Computing Center's long-term archive for documentation
data (https://cera-www.dkrz.de/........, to be specified before publication). The model, scripts used in the analysis and other supplementary
715 information that may be useful in reproducing the authors' work are archived by the Max Planck Institute for Meteorology and can be
obtained by contacting publications@mpimet.mpg.de.

Author contributions. P.d.V designed experiment, performed model adaptation, conducted simulations and analysis, T.S. and T.K performed
model adaptation and conducted parts of the analysis and V.B. was involved in experiment design and conducted parts of the analysis. All
authors reviewed the manuscript.

720 *Competing interests.* The authors declare that they have no competing financial interest.

Acknowledgements. This work was funded by the German Ministry of Education and Research as part of the KoPf-Project (BMBF Grant
No. 03F0764C).

References

Ahn, H., Sauer, T., Richard, T., and Glanville, T.: Determination of thermal properties of composting bulking materials, Bioresource Technology, 100, 3974–3981, https://doi.org/10.1016/j.biortech.2008.11.056, https://doi.org/10.1016/j.biortech.2008.11.056, 2009.

Andresen, C. G., Lawrence, D. M., Wilson, C. J., McGuire, A. D., Koven, C., Schaefer, K., Jafarov, E., Peng, S., Chen, X., Gouttevin, I., Burke, E., Chadburn, S., Ji, D., Chen, G., Hayes, D., and Zhang, W.: Soil Moisture and Hydrology Projections of the Permafrost Region: A Model Intercomparison, The Cryosphere Discussions, pp. 1–20, https://doi.org/10.5194/tc-2019-144, https://doi.org/10.5194/tc-2019-144, 2019.

Batjes, N.: Harmonized soil property values for broad-scale modelling (WISE30sec) with estimates of global soil carbon stocks, Geoderma, 269, 61–68, https://doi.org/10.1016/j.geoderma.2016.01.034, https://doi.org/10.1016/j.geoderma.2016.01.034, 2016.

Batjes, N. H.: Harmonized soil profile data for applications at global and continental scales: updates to the WISE database, Soil Use and Management, 25, 124–127, https://doi.org/10.1111/j.1475-2743.2009.00202.x, https://doi.org/10.1111/j.1475-2743.2009.00202.x, 2009.

Berg, A., Sheffield, J., and Milly, P. C. D.: Divergent surface and total soil moisture projections under global warming, Geophysical Research Letters, 44, 236–244, https://doi.org/10.1002/2016gl071921, https://doi.org/10.1002/2016gl071921, 2017.

Beringer, J., Lynch, A. H., Chapin, F. S., Mack, M., and Bonan, G. B.: The Representation of Arctic Soils in the Land Surface Model: The Importance of Mosses, Journal of Climate, 14, 3324–3335, https://doi.org/10.1175/1520-0442(2001)014<3324:troasi>2.0.co;2, https://doi.org/10.1175/1520-0442(2001)014<3324:troasi>2.0.co;2, 2001.

Beven, K. J. and Kirkby, M. J.: A physically based, variable contributing area model of basin hydrology, Hydrological Sciences Journal, 24, 43–69, 1979.

Biskaborn, B. K., Smith, S. L., Noetzli, J., Matthes, H., Vieira, G., Streletskiy, D. A., Schoeneich, P., Romanovsky, V. E., Lewkowicz, A. G., Abramov, A., Allard, M., Boike, J., Cable, W. L., Christiansen, H. H., Delaloye, R., Diekmann, B., Drozdov, D., Etzelmüller, B., Grosse, G., Guglielmin, M., Ingeman-Nielsen, T., Isaksen, K., Ishikawa, M., Johansson, M., Johannsson, H., Joo, A., Kaverin, D., Kholodov, A., Konstantinov, P., Kröger, T., Lambiel, C., Lanckman, J.-P., Luo, D., Malkova, G., Meiklejohn, I., Moskalenko, N., Oliva, M., Phillips, M., Ramos, M., Sannel, A. B. K., Sergeev, D., Seybold, C., Skryabin, P., Vasiliev, A., Wu, Q., Yoshikawa, K., Zheleznyak, M., and Lantuit, H.: Permafrost is warming at a global scale, Nature Communications, 10, https://doi.org/10.1038/s41467-018-08240-4, https://doi.org/10.1038/s41467-018-08240-4, 2019.

Boucher, O., Halloran, P. R., Burke, E. J., Doutriaux-Boucher, M., Jones, C. D., Lowe, J., Ringer, M. A., Robertson, E., and Wu, P.: Reversibility in an Earth System model in response to CO2concentration changes, Environmental Research Letters, 7, 024 013, https://doi.org/10.1088/1748-9326/7/2/024013, https://doi.org/10.1088/1748-9326/7/2/024013, 2012.

Brown, J. and Romanovsky, V. E.: Report from the International Permafrost Association: state of permafrost in the first decade of the 21st century, Permafrost and Periglacial Processes, 19, 255–260, https://doi.org/10.1002/ppp.618, https://doi.org/10.1002/ppp.618, 2008.

Burke, E. J., Hartley, I. P., and Jones, C. D.: Uncertainties in the global temperature change caused by carbon release from permafrost thawing, The Cryosphere, 6, 1063–1076, https://doi.org/10.5194/tc-6-1063-2012, https://doi.org/10.5194/tc-6-1063-2012, 2012.

Burke, E. J., Chadburn, S. E., and Ekici, A.: A vertical representation of soil carbon in the JULES land surface scheme (vn4.3_permafrost) with a focus on permafrost regions, Geoscientific Model Development, 10, 959–975, https://doi.org/10.5194/gmd-10-959-2017, https://doi.org/10.5194/gmd-10-959-2017, 2017a.

Burke, E. J., Ekici, A., Huang, Y., Chadburn, S. E., Huntingford, C., Ciais, P., Friedlingstein, P., Peng, S., and Krinner, G.: Quantifying uncertainties of permafrost carbon–climate feedbacks, Biogeosciences, 14, 3051–3066, https://doi.org/10.5194/bg-14-3051-2017, https://doi.org/10.5194/bg-14-3051-2017, 2017b.

Burke, E. J., Chadburn, S. E., Huntingford, C., and Jones, C. D.: CO2 loss by permafrost thawing implies additional emissions reductions to limit warming to 1.5 or 2 °C, Environmental Research Letters, 13, 024 024, https://doi.org/10.1088/1748-9326/aaa138, https://doi.org/10.1088/1748-9326/aaa138, 2018.

Callaghan, T. V., Bergholm, F., Christensen, T. R., Jonasson, C., Kokfelt, U., and Johansson, M.: A new climate era in the sub-Arctic: Accelerating climate changes and multiple impacts, Geophysical Research Letters, 37, n/a–n/a, https://doi.org/10.1029/2009gl042064, https://doi.org/10.1029/2009gl042064, 2010.

Chadburn, S. E., Krinner, G., Porada, P., Bartsch, A., Beer, C., Marchesini, L. B., Boike, J., Ekici, A., Elberling, B., Friborg, T., Hugelius, G., Johansson, M., Kuhry, P., Kutzbach, L., Langer, M., Lund, M., Parmentier, F.-J. W., Peng, S., Huissteden, K. V., Wang, T., Westermann, S., Zhu, D., and Burke, E. J.: Carbon stocks and fluxes in the high latitudes: using site-level data to evaluate Earth system models, Biogeosciences, 14, 5143–5169, https://doi.org/10.5194/bg-14-5143-2017, https://doi.org/10.5194/bg-14-5143-2017, 2017.

Chojnacky, D., Amacher, M., and Gavazzi, M.: Separating Duff and Litter for Improved Mass and Carbon Estimates, Southern Journal of Applied Forestry, 33, 29–34, https://doi.org/10.1093/sjaf/33.1.29, https://doi.org/10.1093/sjaf/33.1.29, 2009.

Comyn-Platt, E., Hayman, G., Huntingford, C., Chadburn, S. E., Burke, E. J., Harper, A. B., Collins, W. J., Webber, C. P., Powell, T., Cox, P. M., Gedney, N., and Sitch, S.: Carbon budgets for 1.5 and 2 °C targets lowered by natural wetland and permafrost feedbacks, Nature Geoscience, 11, 568–573, https://doi.org/10.1038/s41561-018-0174-9, https://doi.org/10.1038/s41561-018-0174-9, 2018.

Dümenil, L. and Todini, E.: A rainfall-runoff scheme for use in the Hamburg climate model, ,J.P. O'Kane (Ed.): Advances in Theoretical Hydrology, A Tribune to James Dooge,, pp. 129–157, 1992.

Ekici, A., Beer, C., Hagemann, S., Boike, J., Langer, M., and Hauck, C.: Simulating high-latitude permafrost regions by the JSBACH terrestrial ecosystem model, Geosci. Model Dev., 7, 631–647, 2014.

Ekici, A., Chadburn, S., Chaudhary, N., Hajdu, L. H., Marmy, A., Peng, S., Boike, J., Burke, E., Friend, A. D., Hauck, C., Krinner, G., Langer, M., Miller, P. A., and Beer, C.: Site-level model intercomparison of high latitude and high altitude soil thermal dynamics in tundra and barren landscapes, The Cryosphere, 9, 1343–1361, https://doi.org/10.5194/tc-9-1343-2015, https://doi.org/10.5194/tc-9-1343-2015, 2015.

Elberling, B., Michelsen, A., Schaedel, C., Schuur, E. A. G., Christiansen, H. H., Berg, L., Tamstorf, M. P., and Sigsgaard, C.: Long-term CO2 production following permafrost thaw, Nature Climate Change, 3, 890–894, https://doi.org/10.1038/nclimate1955, https://doi.org/10.1038/nclimate1955, 2013.

Eliseev, A. V., Demchenko, P. F., Arzhanov, M. M., and Mokhov, I. I.: Transient hysteresis of near-surface permafrost response to external forcing, Climate Dynamics, 42, 1203–1215, https://doi.org/10.1007/s00382-013-1672-5, https://doi.org/10.1007/s00382-013-1672-5, 2013.

Etzelmueller, B., Schuler, T. V., Isaksen, K., Christiansen, H. H., Farbrot, H., and Benestad, R.: Modeling the temperature evolution of Svalbard permafrost during the 20th and 21st century, The Cryosphere, 5, 67–79, https://doi.org/10.5194/tc-5-67-2011, https://doi.org/10.5194/tc-5-67-2011, 2011.

Eyring, V., Bony, S., Meehl, G. A., Senior, C. A., Stevens, B., Stouffer, R. J., and Taylor, K. E.: Overview of the Coupled Model Intercomparison Project Phase 6 (CMIP6) experimental design and organization, Geoscientific Model Development, 9, 1937–1958, https://doi.org/10.5194/gmd-9-1937-2016, https://doi.org/10.5194/gmd-9-1937-2016, 2016.

Frauenfeld, O. W.: Interdecadal changes in seasonal freeze and thaw depths in Russia, Journal of Geophysical Research, 109, https://doi.org/10.1029/2003jd004245, https://doi.org/10.1029/2003jd004245, 2004.

Geden, O. and Löschel, A.: Define limits for temperature overshoot targets, Nature Geoscience, 10, 881–882, https://doi.org/10.1038/s41561-017-0026-z, https://doi.org/10.1038/s41561-017-0026-z, 2017.

800 Gilichinsky, D., Rivkina, E., Shcherbakova, V., Laurinavichuis, K., and Tiedje, J.: Supercooled Water Brines Within Permafrost—An Unknown Ecological Niche for Microorganisms: A Model for Astrobiology, Astrobiology, 3, 331–341, https://doi.org/10.1089/153110703769016424, https://doi.org/10.1089/153110703769016424, 2003.

Hagemann, S. and Stacke, T.: Impact of the soil hydrology scheme on simulated soil moisture memory, Climate Dynamics, 44, 1731–1750, https://doi.org/10.1007/s00382-014-2221-6, https://doi.org/10.1007/s00382-014-2221-6, 2015.

805 Hagemann, S., Göttel, H., Jacob, D., Lorenz, P., and Roeckner, E.: Improved regional scale processes reflected in projected hydrological changes over large European catchments, Clim. Dyn., 32, 767–781, 2009.

Hugelius, G., Bockheim, J. G., Camill, P., Elberling, B., Grosse, G., Harden, J. W., Johnson, K., Jorgenson, T., Koven, C. D., Kuhry, P., Michaelson, G., Mishra, U., Palmtag, J., Ping, C.-L., O'Donnell, J., Schirrmeister, L., Schuur, E. A. G., Sheng, Y., Smith, L. C., Strauss, J., and Yu, Z.: A new data set for estimating organic carbon storage to 3 m depth in soils of the northern circumpolar permafrost region,

810 Earth System Science Data, 5, 393–402, https://doi.org/10.5194/essd-5-393-2013, https://doi.org/10.5194/essd-5-393-2013, 2013.

Hugelius, G., Strauss, J., Zubrzycki, S., Harden, J. W., Schuur, E. A. G., Ping, C.-L., Schirrmeister, L., Grosse, G., Michaelson, G. J., Koven, C. D., O'Donnell, J. A., Elberling, B., Mishra, U., Camill, P., Yu, Z., Palmtag, J., and Kuhry, P.: Estimated stocks of circumpolar permafrost carbon with quantified uncertainty ranges and identified data gaps, Biogeosciences, 11, 6573–6593, https://doi.org/10.5194/bg-11-6573-2014, https://doi.org/10.5194/bg-11-6573-2014, 2014.

815 Huntingford, C. and Lowe, J.: "Overshoot" Scenarios and Climate Change, Science, 316, 829b–829b, https://doi.org/10.1126/science.316.5826.829b, https://doi.org/10.1126/science.316.5826.829b, 2007.

Isaksen, K., Sollid, J. L., Holmlund, P., and Harris, C.: Recent warming of mountain permafrost in Svalbard and Scandinavia, Journal of Geophysical Research, 112, https://doi.org/10.1029/2006jf000522, https://doi.org/10.1029/2006jf000522, 2007.

Jackson, R., Canadell, J., Ehleringer, J. R., Mooney, H., Sala, O., and Schulze, E. D.: A global analysis of root distributions for terrestrial

820 biomes, Oecologia, 108, 389–411, 1996.

Jafarov, E. and Schaefer, K.: The importance of a surface organic layer in simulating permafrost thermal and carbon dynamics, The Cryosphere, 10, 465–475, https://doi.org/10.5194/tc-10-465-2016, https://doi.org/10.5194/tc-10-465-2016, 2016.

Johnstone, J. F., Chapin, F. S., Hollingsworth, T. N., Mack, M. C., Romanovsky, V., and Turetsky, M.: Fire, climate change, and forest resilience in interior AlaskaThis article is one of a selection of papers from The Dynamics of Change in Alaska's Boreal Forests: Resilience

825 and Vulnerability in Response to Climate Warming., Canadian Journal of Forest Research, 40, 1302–1312, https://doi.org/10.1139/x10-061, https://doi.org/10.1139/x10-061, 2010.

Keenan, T. F. and Riley, W. J.: Greening of the land surface in the world's cold regions consistent with recent warming, Nature Climate Change, 8, 825–828, https://doi.org/10.1038/s41558-018-0258-y, https://doi.org/10.1038/s41558-018-0258-y, 2018.

Kelly, R. H., Parton, W. J., Hartman, M. D., Stretch, L. K., Ojima, D. S., and Schimel, D. S.: Intra-annual and interannual

830 variability of ecosystem processes in shortgrass steppe, Journal of Geophysical Research: Atmospheres, 105, 20 093–20 100, https://doi.org/10.1029/2000jd900259, https://doi.org/10.1029/2000jd900259, 2000.

Khvorostyanov, D. V., Ciais, P., Krinner, G., and Zimov, S. A.: Vulnerability of east Siberia's frozen carbon stores to future warming, Geophysical Research Letters, 35, https://doi.org/10.1029/2008gl033639, https://doi.org/10.1029/2008gl033639, 2008a.

Khvorostyanov, D. V., Krinner, G., Ciais, P., Heimann, M., and Zimov, S. A.: Vulnerability of permafrost carbon to global warming. Part
835   I: model description and role of heat generated by organic matter decomposition, Tellus B: Chemical and Physical Meteorology, 60,
       250–264, https://doi.org/10.1111/j.1600-0889.2007.00333.x, https://doi.org/10.1111/j.1600-0889.2007.00333.x, 2008b.

Kleinen, T., Mikolajewicz, U., and Brovkin, V.: Terrestrial methane emissions from Last Glacial Maximum to preindustrial, Clim. Past
       Discuss., https://doi.org/10.5194/cp-2019-109, https://doi.org/10.5194/cp-2019-109, in review, 2019.

Koven, C., Friedlingstein, P., Ciais, P., Khvorostyanov, D., Krinner, G., and Tarnocai, C.: On the formation of high-latitude soil car-
840   bon stocks: Effects of cryoturbation and insulation by organic matter in a land surface model, Geophysical Research Letters, 36,
       https://doi.org/10.1029/2009gl040150, https://doi.org/10.1029/2009gl040150, 2009.

Koven, C. D., Riley, W. J., Subin, Z. M., Tang, J. Y., Torn, M. S., Collins, W. D., Bonan, G. B., Lawrence, D. M., and Swenson, S. C.:
       The effect of vertically resolved soil biogeochemistry and alternate soil C and N models on C dynamics of CLM4, Biogeosciences, 10,
       7109–7131, https://doi.org/10.5194/bg-10-7109-2013, https://doi.org/10.5194/bg-10-7109-2013, 2013.

845 Koven, C. D., Lawrence, D. M., and Riley, W. J.: Permafrost carbon-climate feedback is sensitive to deep soil carbon decomposability but not
       deep soil nitrogen dynamics, Proceedings of the National Academy of Sciences, p. 201415123, https://doi.org/10.1073/pnas.1415123112,
       https://doi.org/10.1073/pnas.1415123112, 2015.

Lawrence, D. M., Slater, A. G., Romanovsky, V. E., and Nicolsky, D. J.: Sensitivity of a model projection of near-surface per-
       mafrost degradation to soil column depth and representation of soil organic matter, Journal of Geophysical Research, 113,
850   https://doi.org/10.1029/2007jf000883, https://doi.org/10.1029/2007jf000883, 2008.

Lawrence, D. M., Koven, C. D., Swenson, S. C., Riley, W. J., and Slater, A. G.: Permafrost thaw and resulting soil moisture changes
       regulate projected high-latitude CO2and CH4emissions, Environmental Research Letters, 10, 094 011, https://doi.org/10.1088/1748-
       9326/10/9/094011, https://doi.org/10.1088/1748-9326/10/9/094011, 2015.

Liski, J., Palosuo, T., Peltoniemi, M., and Sievänen, R.: Carbon and decomposition model Yasso for forest soils, Ecological Modelling, 189,
855   168–182, https://doi.org/10.1016/j.ecolmodel.2005.03.005, https://doi.org/10.1016/j.ecolmodel.2005.03.005, 2005.

MacDougall, A. H., Avis, C. A., and Weaver, A. J.: Significant contribution to climate warming from the permafrost carbon feedback, Nature
       Geoscience, 5, 719–721, https://doi.org/10.1038/ngeo1573, https://doi.org/10.1038/ngeo1573, 2012.

Marthews, T. R., Dadson, S. J., Lehner, B., Abele, S., and Gedney, N.: High-resolution global topographic index values for use in large-scale
       hydrological modelling, Hydrology and Earth System Sciences, 19, 91–104, https://doi.org/10.5194/hess-19-91-2015, https://doi.org/10.
860   5194/hess-19-91-2015, 2015.

Mauritsen, T., Bader, J., Becker, T., Behrens, J., Bittner, M., Brokopf, R., Brovkin, V., Claussen, M., Crueger, T., Esch, M., Fast, I., Fiedler,
       S., Fläschner, D., Gayler, V., Giorgetta, M., Goll, D. S., Haak, H., Hagemann, S., Hedemann, C., Hohenegger, C., Ilyina, T., Jahns,
       T., Jimenez-de-la Cuesta, D., Jungclaus, J., Kleinen, T., Kloster, S., Kracher, D., Kinne, S., Kleberg, D., Lasslop, G., Kornblueh, L.,
       Marotzke, J., Matei, D., Meraner, K., Mikolajewicz, U., Modali, K., Möbis, B., Müller, W. A., Nabel, J. E. M. S., Nam, C. C. W., Notz,
865   D., Nyawira, S.-S., Paulsen, H., Peters, K., Pincus, R., Pohlmann, H., Pongratz, J., Popp, M., Raddatz, T. J., Rast, S., Redler, R., Reick,
       C. H., Rohrschneider, T., Schemann, V., Schmidt, H., Schnur, R., Schulzweida, U., Six, K. D., Stein, L., Stemmler, I., Stevens, B., von
       Storch, J.-S., Tian, F., Voigt, A., Vrese, P., Wieners, K.-H., Wilkenskjeld, S., Winkler, A., and Roeckner, E.: Developments in the MPI-M
       Earth System Model version 1.2 (MPI-ESM1.2) and Its Response to Increasing CO2, Journal of Advances in Modeling Earth Systems,
       11, 998–1038, https://doi.org/10.1029/2018MS001400, https://agupubs.onlinelibrary.wiley.com/doi/abs/10.1029/2018MS001400, 2019.

870 McGuire, A. D., Koven, C., Lawrence, D. M., Clein, J. S., Xia, J., Beer, C., Burke, E., Chen, G., Chen, X., Delire, C., Jafarov, E., MacDougall,
       A. H., Marchenko, S., Nicolsky, D., Peng, S., Rinke, A., Saito, K., Zhang, W., Alkama, R., Bohn, T. J., Ciais, P., Decharme, B., Ekici,

A., Gouttevin, I., Hajima, T., Hayes, D. J., Ji, D., Krinner, G., Lettenmaier, D. P., Luo, Y., Miller, P. A., Moore, J. C., Romanovsky, V., Schädel, C., Schaefer, K., Schuur, E. A., Smith, B., Sueyoshi, T., and Zhuang, Q.: Variability in the sensitivity among model simulations of permafrost and carbon dynamics in the permafrost region between 1960 and 2009, Global Biogeochemical Cycles, 30, 1015–1037,
875   https://doi.org/10.1002/2016gb005405, https://doi.org/10.1002/2016gb005405, 2016.

McGuire, A. D., Lawrence, D. M., Koven, C., Clein, J. S., Burke, E., Chen, G., Jafarov, E., MacDougall, A. H., Marchenko, S., Nicolsky, D., Peng, S., Rinke, A., Ciais, P., Gouttevin, I., Hayes, D. J., Ji, D., Krinner, G., Moore, J. C., Romanovsky, V., Schädel, C., Schaefer, K., Schuur, E. A. G., and Zhuang, Q.: Dependence of the evolution of carbon dynamics in the northern permafrost region on the trajectory of climate change, Proceedings of the National Academy of Sciences, 115, 3882–3887, https://doi.org/10.1073/pnas.1719903115, https:
880   //doi.org/10.1073/pnas.1719903115, 2018.

Nicolsky, D. J., Romanovsky, V. E., Tipenko, G. S., and Walker, D. A.: Modeling biogeophysical interactions in nonsorted circles in the Low Arctic, Journal of Geophysical Research, 113, https://doi.org/10.1029/2007jg000565, https://doi.org/10.1029/2007jg000565, 2008.

Niu, G.-Y. and Yang, Z.-L.: Effects of Frozen Soil on Snowmelt Runoff and Soil Water Storage at a Continental Scale, Journal of Hydrometeorology, 7, 937–952, https://doi.org/10.1175/jhm538.1, https://doi.org/10.1175/jhm538.1, 2006.

885 Nusbaumer, J. and Matsumoto, K.: Climate and carbon cycle changes under the overshoot scenario, Global and Planetary Change, 62, 164–172, https://doi.org/10.1016/j.gloplacha.2008.01.002, https://doi.org/10.1016/j.gloplacha.2008.01.002, 2008.

Oberbauer, S. F., Tweedie, C. E., Welker, J. M., Fahnestock, J. T., Henry, G. H. R., Webber, P. J., Hollister, R. D., Walker, M. D., Kuchy, A., Elmore, E., and Starr, G.: TUNDRA CO2FLUXES IN RESPONSE TO EXPERIMENTAL WARMING ACROSS LATITUDINAL AND MOISTURE GRADIENTS, Ecological Monographs, 77, 221–238, https://doi.org/10.1890/06-0649, https://doi.org/10.1890/06-0649,
890   2007.

O'Donnell, J. A., Romanovsky, V. E., Harden, J. W., and McGuire, A. D.: The Effect of Moisture Content on the Thermal Conductivity of Moss and Organic Soil Horizons From Black Spruce Ecosystems in Interior Alaska, Soil Science, 174, 646–651, https://doi.org/10.1097/ss.0b013e3181c4a7f8, https://doi.org/10.1097/ss.0b013e3181c4a7f8, 2009.

Oh, Y., Zhuang, Q., Liu, L., Welp, L. R., Lau, M. C. Y., Onstott, T. C., Medvigy, D., Bruhwiler, L., Dlugokencky, E. J., Hugelius, G.,
895   D'Imperio, L., and Elberling, B.: Reduced net methane emissions due to microbial methane oxidation in a warmer Arctic, Nature Climate Change, 10, 317–321, https://doi.org/10.1038/s41558-020-0734-z, https://doi.org/10.1038/s41558-020-0734-z, 2020.

Olefeldt, D., Turetsky, M. R., Crill, P. M., and McGuire, A. D.: Environmental and physical controls on northern terrestrial methane emissions across permafrost zones, Global Change Biology, 19, 589–603, https://doi.org/10.1111/gcb.12071, https://doi.org/10.1111/gcb.12071, 2012.

900 Oleson, K., Lawrence, D., Bonan, G., Drewniak, B., Huang, M., Charles, D., Levis, S., Li, F., Riley, W., Zachary, M., et al.: Technical Description of version 4.5 of the Community Land Model (CLM) Coordinating, BOULDER, COLORADO, pp. 80 307–3000, 2013.

Osterkamp, T. E.: Characteristics of the recent warming of permafrost in Alaska, Journal of Geophysical Research, 112, https://doi.org/10.1029/2006jf000578, https://doi.org/10.1029/2006jf000578, 2007.

Parry, M., Lowe, J., and Hanson, C.: Overshoot, adapt and recover, Nature, 458, 1102–1103, https://doi.org/10.1038/4581102a, https://doi.
905   org/10.1038/4581102a, 2009.

Pearson, R. G., Phillips, S. J., Loranty, M. M., Beck, P. S. A., Damoulas, T., Knight, S. J., and Goetz, S. J.: Shifts in Arctic vegetation and associated feedbacks under climate change, Nature Climate Change, 3, 673–677, https://doi.org/10.1038/nclimate1858, https://doi.org/10.1038/nclimate1858, 2013.

Peters-Lidard, C., Blackburn, E., Liang, X., and Wood, E. F.: The effect of soil thermal conductivity parameterization on surface energy fluxes and temperatures, Journal of the Atmospheric Sciences, 55, 1209–1224, 1998.

Peterson, R., Walker, D., Romanovsky, V., Knudson, J., Raynolds, M., and Krantz, W.: A differential frost heave model: cryoturbation-vegetation interactions, Proceedings of the Eighth International Conference on Permafrost, 2, 885–890, 2003.

Qian, H., Joseph, R., and Zeng, N.: Enhanced terrestrial carbon uptake in the Northern High Latitudes in the 21st century from the Coupled Carbon Cycle Climate Model Intercomparison Project model projections, Global Change Biology, 16, 641–656, https://doi.org/10.1111/j.1365-2486.2009.01989.x, https://doi.org/10.1111/j.1365-2486.2009.01989.x, 2010.

Quéré, C. L., Andrew, R. M., Friedlingstein, P., Sitch, S., Pongratz, J., Manning, A. C., Korsbakken, J. I., Peters, G. P., Canadell, J. G., Jackson, R. B., Boden, T. A., Tans, P. P., Andrews, O. D., Arora, V. K., Bakker, D. C. E., Barbero, L., Becker, M., Betts, R. A., Bopp, L., Chevallier, F., Chini, L. P., Ciais, P., Cosca, C. E., Cross, J., Currie, K., Gasser, T., Harris, I., Hauck, J., Haverd, V., Houghton, R. A., Hunt, C. W., Hurtt, G., Ilyina, T., Jain, A. K., Kato, E., Kautz, M., Keeling, R. F., Goldewijk, K. K., Körtzinger, A., Landschützer, P., Lefèvre, N., Lenton, A., Lienert, S., Lima, I., Lombardozzi, D., Metzl, N., Millero, F., Monteiro, P. M. S., Munro, D. R., Nabel, J. E. M. S., ichiro Nakaoka, S., Nojiri, Y., Padin, X. A., Peregon, A., Pfeil, B., Pierrot, D., Poulter, B., Rehder, G., Reimer, J., Rödenbeck, C., Schwinger, J., Séférian, R., Skjelvan, I., Stocker, B. D., Tian, H., Tilbrook, B., Tubiello, F. N., van der Laan-Luijkx, I. T., van der Werf, G. R., van Heuven, S., Viovy, N., Vuichard, N., Walker, A. P., Watson, A. J., Wiltshire, A. J., Zaehle, S., and Zhu, D.: Global Carbon Budget 2017, Earth System Science Data, 10, 405–448, https://doi.org/10.5194/essd-10-405-2018, https://doi.org/10.5194/essd-10-405-2018, 2018.

Riahi, K., van Vuuren, D. P., Kriegler, E., Edmonds, J., O'Neill, B. C., Fujimori, S., Bauer, N., Calvin, K., Dellink, R., Fricko, O., Lutz, W., Popp, A., Cuaresma, J. C., KC, S., Leimbach, M., Jiang, L., Kram, T., Rao, S., Emmerling, J., Ebi, K., Hasegawa, T., Havlik, P., Humpenöder, F., Silva, L. A. D., Smith, S., Stehfest, E., Bosetti, V., Eom, J., Gernaat, D., Masui, T., Rogelj, J., Strefler, J., Drouet, L., Krey, V., Luderer, G., Harmsen, M., Takahashi, K., Baumstark, L., Doelman, J. C., Kainuma, M., Klimont, Z., Marangoni, G., Lotze-Campen, H., Obersteiner, M., Tabeau, A., and Tavoni, M.: The Shared Socioeconomic Pathways and their energy, land use, and greenhouse gas emissions implications: An overview, Global Environmental Change, 42, 153–168, https://doi.org/10.1016/j.gloenvcha.2016.05.009, https://doi.org/10.1016/j.gloenvcha.2016.05.009, 2017.

Riley, W. J., Subin, Z. M., Lawrence, D. M., Swenson, S. C., Torn, M. S., Meng, L., Mahowald, N. M., and Hess, P.: Barriers to predicting changes in global terrestrial methane fluxes: analyses using CLM4Me, a methane biogeochemistry model integrated in CESM, Biogeosciences, 8, 1925–1953, https://doi.org/10.5194/bg-8-1925-2011, https://doi.org/10.5194/bg-8-1925-2011, 2011.

Romanovsky, V. E., Drozdov, D. S., Oberman, N. G., Malkova, G. V., Kholodov, A. L., Marchenko, S. S., Moskalenko, N. G., Sergeev, D. O., Ukraintseva, N. G., Abramov, A. A., Gilichinsky, D. A., and Vasiliev, A. A.: Thermal state of permafrost in Russia, Permafrost and Periglacial Processes, 21, 136–155, https://doi.org/10.1002/ppp.683, https://doi.org/10.1002/ppp.683, 2010.

Schaedel, C., Bader, M. K.-F., Schuur, E. A. G., Biasi, C., Bracho, R., Čapek, P., Baets, S. D., Diáková, K., Ernakovich, J., Estop-Aragones, C., Graham, D. E., Hartley, I. P., Iversen, C. M., Kane, E., Knoblauch, C., Lupascu, M., Martikainen, P. J., Natali, S. M., Norby, R. J., O'Donnell, J. A., Chowdhury, T. R., Šantrůčková, H., Shaver, G., Sloan, V. L., Treat, C. C., Turetsky, M. R., Waldrop, M. P., and Wickland, K. P.: Potential carbon emissions dominated by carbon dioxide from thawed permafrost soils, Nature Climate Change, 6, 950–953, https://doi.org/10.1038/nclimate3054, https://doi.org/10.1038/nclimate3054, 2016.

Schaefer, K., Zhang, T., Bruhwiler, L., and Barrett, A. P.: Amount and timing of permafrost carbon release in response to climate warming, Tellus B, 63, 165–180, https://doi.org/10.1111/j.1600-0889.2011.00527.x, https://doi.org/10.1111/j.1600-0889.2011.00527.x, 2011.

945   Schaefer, K., Lantuit, H., Romanovsky, V. E., Schuur, E. A. G., and Witt, R.: The impact of the permafrost carbon feedback on global climate, Environmental Research Letters, 9, 085 003, https://doi.org/10.1088/1748-9326/9/8/085003, https://doi.org/10.1088/1748-9326/9/8/085003, 2014.

Schuur, E. A. G., Bockheim, J., Canadell, J. G., Euskirchen, E., Field, C. B., Goryachkin, S. V., Hagemann, S., Kuhry, P., Lafleur, P. M., Lee, H., Mazhitova, G., Nelson, F. E., Rinke, A., Romanovsky, V. E., Shiklomanov, N., Tarnocai, C., Venevsky, S., Vogel, J. G., and Zimov,

950   S. A.: Vulnerability of Permafrost Carbon to Climate Change: Implications for the Global Carbon Cycle, BioScience, 58, 701–714, https://doi.org/10.1641/b580807, https://doi.org/10.1641/b580807, 2008.

Schuur, E. A. G., Abbott, B. W., Bowden, W. B., Brovkin, V., Camill, P., Canadell, J. G., Chanton, J. P., Chapin, F. S., Christensen, T. R., Ciais, P., Crosby, B. T., Czimczik, C. I., Grosse, G., Harden, J., Hayes, D. J., Hugelius, G., Jastrow, J. D., Jones, J. B., Kleinen, T., Koven, C. D., Krinner, G., Kuhry, P., Lawrence, D. M., McGuire, A. D., Natali, S. M., O'Donnell, J. A., Ping, C. L., Riley, W. J., Rinke, A.,

955   Romanovsky, V. E., Sannel, A. B. K., Schädel, C., Schaefer, K., Sky, J., Subin, Z. M., Tarnocai, C., Turetsky, M. R., Waldrop, M. P., Anthony, K. M. W., Wickland, K. P., Wilson, C. J., and Zimov, S. A.: Expert assessment of vulnerability of permafrost carbon to climate change, Climatic Change, 119, 359–374, https://doi.org/10.1007/s10584-013-0730-7, https://doi.org/10.1007/s10584-013-0730-7, 2013.

Schuur, E. A. G., McGuire, A. D., Schädel, C., Grosse, G., Harden, J. W., Hayes, D. J., Hugelius, G., Koven, C. D., Kuhry, P., Lawrence, D. M., Natali, S. M., Olefeldt, D., Romanovsky, V. E., Schaefer, K., Turetsky, M. R., Treat, C. C., and Vonk, J. E.: Climate change and the

960   permafrost carbon feedback, Nature, 520, 171–179, https://doi.org/10.1038/nature14338, https://doi.org/10.1038/nature14338, 2015.

Shiklomanov, N. I., Streletskiy, D. A., Nelson, F. E., Hollister, R. D., Romanovsky, V. E., Tweedie, C. E., Bockheim, J. G., and Brown, J.: Decadal variations of active-layer thickness in moisture-controlled landscapes, Barrow, Alaska, Journal of Geophysical Research, 115, https://doi.org/10.1029/2009jg001248, https://doi.org/10.1029/2009jg001248, 2010.

Sierra, C. A., Trumbore, S. E., Davidson, E. A., Vicca, S., and Janssens, I.: Sensitivity of decomposition rates of soil organic mat-

965   ter with respect to simultaneous changes in temperature and moisture, Journal of Advances in Modeling Earth Systems, 7, 335–356, https://doi.org/10.1002/2014ms000358, https://doi.org/10.1002/2014ms000358, 2015.

Stacke, T. and Hagemann, S.: Development and evaluation of a global dynamical wetlands extent scheme, Hydrology and Earth System Sciences, 16, 2915–2933, https://doi.org/10.5194/hess-16-2915-2012, 2012.

Stocker, T., Qin, D., Plattner, G.-K., Alexander, L., Allen, S., Bindoff, N., Bren, F.-M., Church, J., Cubasch, U., Emori, S., Forster, P.,

970   Friedlingstein, P., Gillett, N., Gregory, J., Hartmann, D., Jansen, E., Kirtman, B., Knutti, R., Krishna Kumar, K., Lemke, P., Marotzke, J., Masson-Delmotte, V., Meehl, G., Mokhov, I., Piao, S., Ramaswamy, V., Randall, D., Rhein, M., Rojas, M., Sabine, C., Shindell, D., Talley, L., Vaughan, D., and Xie, S.-P.: Technical Summary, Book section, Cambridge, United Kingdom and New York, NY, USA, https://doi.org/10.1017/CBO9781107415324.005, www.climatechange2013.org, 2013.

Tarnocai, C., Canadell, J. G., Schuur, E. A. G., Kuhry, P., Mazhitova, G., and Zimov, S.: Soil organic carbon pools in the northern cir-

975   cumpolar permafrost region, Global Biogeochemical Cycles, 23, n/a–n/a, https://doi.org/10.1029/2008gb003327, https://doi.org/10.1029/2008gb003327, 2009.

Todini, E.: The ARNO rainfall—runoff model, Journal of Hydrology, 175, 339–382, https://doi.org/10.1016/s0022-1694(96)80016-3, https://doi.org/10.1016/s0022-1694(96)80016-3, 1996.

Tuomi, M., Rasinmäki, J., Repo, A., Vanhala, P., and Liski, J.: Soil carbon model Yasso07 graphical user interface, Environmental Modelling

980   & Software, 26, 1358–1362, https://doi.org/10.1016/j.envsoft.2011.05.009, https://doi.org/10.1016/j.envsoft.2011.05.009, 2011.

van Vuuren, D. P., Edmonds, J., Kainuma, M., Riahi, K., Thomson, A., Hibbard, K., Hurtt, G. C., Kram, T., Krey, V., Lamarque, J.-F., and et al.: The representative concentration pathways: an overview, Climatic Change, 109, 5–31, https://doi.org/10.1007/s10584-011-0148-z, http://dx.doi.org/10.1007/s10584-011-0148-z, 2011.

von Deimling, T. S., Meinshausen, M., Levermann, A., Huber, V., Frieler, K., Lawrence, D. M., and Brovkin, V.: Estimating the near-surface permafrost-carbon feedback on global warming, Biogeosciences, 9, 649–665, https://doi.org/10.5194/bg-9-649-2012, https://doi.org/10.5194/bg-9-649-2012, 2012.

von Deimling, T. S., Kleinen, T., Hugelius, G., Knoblauch, C., Beer, C., and Brovkin, V.: Long-term deglacial permafrost carbon dynamics in MPI-ESM, Climate of the Past, 14, 2011–2036, https://doi.org/10.5194/cp-14-2011-2018, https://doi.org/10.5194/cp-14-2011-2018, 2018.

Wu, Q. and Zhang, T.: Changes in active layer thickness over the Qinghai-Tibetan Plateau from 1995 to 2007, Journal of Geophysical Research, 115, https://doi.org/10.1029/2009jd012974, https://doi.org/10.1029/2009jd012974, 2010.

Yi, S., Manies, K., Harden, J., and McGuire, A. D.: Characteristics of organic soil in black spruce forests: Implications for the application of land surface and ecosystem models in cold regions, Geophysical Research Letters, 36, https://doi.org/10.1029/2008gl037014, https://doi.org/10.1029/2008gl037014, 2009.

Zhang, W., Miller, P. A., Jansson, C., Samuelsson, P., Mao, J., and Smith, B.: Self-Amplifying Feedbacks Accelerate Greening and Warming of the Arctic, Geophysical Research Letters, 45, 7102–7111, https://doi.org/10.1029/2018gl077830, https://doi.org/10.1029/2018gl077830, 2018.

Zhu, D., Ciais, P., Krinner, G., Maignan, F., Puig, A. J., and Hugelius, G.: Controls of soil organic matter on soil thermal dynamics in the northern high latitudes, Nature Communications, 10, https://doi.org/10.1038/s41467-019-11103-1, https://doi.org/10.1038/s41467-019-11103-1, 2019.

Zimov, S. A.: CLIMATE CHANGE: Permafrost and the Global Carbon Budget, Science, 312, 1612–1613, https://doi.org/10.1126/science.1128908, https://doi.org/10.1126/science.1128908, 2006a.

Zimov, S. A.: CLIMATE CHANGE: Permafrost and the Global Carbon Budget, Science, 312, 1612–1613, https://doi.org/10.1126/science.1128908, https://doi.org/10.1126/science.1128908, 2006b.

Zimov, S. A., Davydov, S. P., Zimova, G. M., Davydova, A. I., Schuur, E. A. G., Dutta, K., and Chapin, F. S.: Permafrost carbon: Stock and decomposability of a globally significant carbon pool, Geophysical Research Letters, 33, https://doi.org/10.1029/2006gl027484, https://doi.org/10.1029/2006gl027484, 2006.
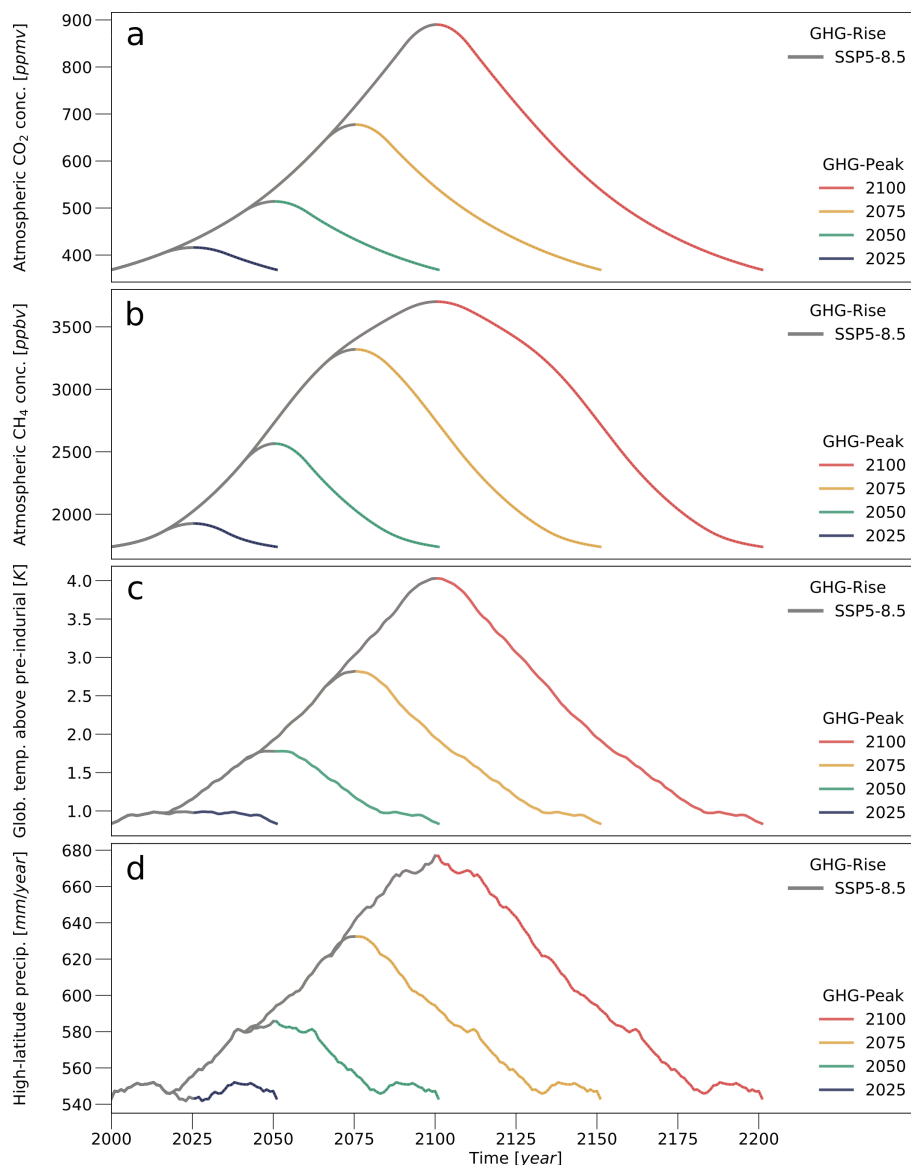
Figure 1. Experimental setup: Forcing used to drive the land-surface model after the 1850 - 2000 spin up phase: **a)** Atmospheric CO_2 concentrations. **b)** Atmospheric CH_4 concentrations. **c)** Global mean surface temperature relative to the pre-industrial temperature. Note that the model is not forced by surface temperatures directly, but by atmospheric temperatures at a height of roughly 30 m and the surface incoming long- and short-wave radiative fluxes. **d)** Precipitation rates, averaged over the latitudinal band between $60°$ and $90°$ North. Grey lines show the forcing according to the SSP5-RCP8.5 scenario. The coloured lines show the forcing-pathways that are used to reverse the forcing to the state at the beginning of the 21st century – after an assumed peak in the year 2025 (blue), 2050 (green), 2075 (yellow) and 2100 (red). In case of temperature (and the surface radiative fluxes) and precipitation rates, the forcing was derived from CMIP6 scenario simulations with the fully coupled MPI-ESM. Shown is the 20-year moving average.
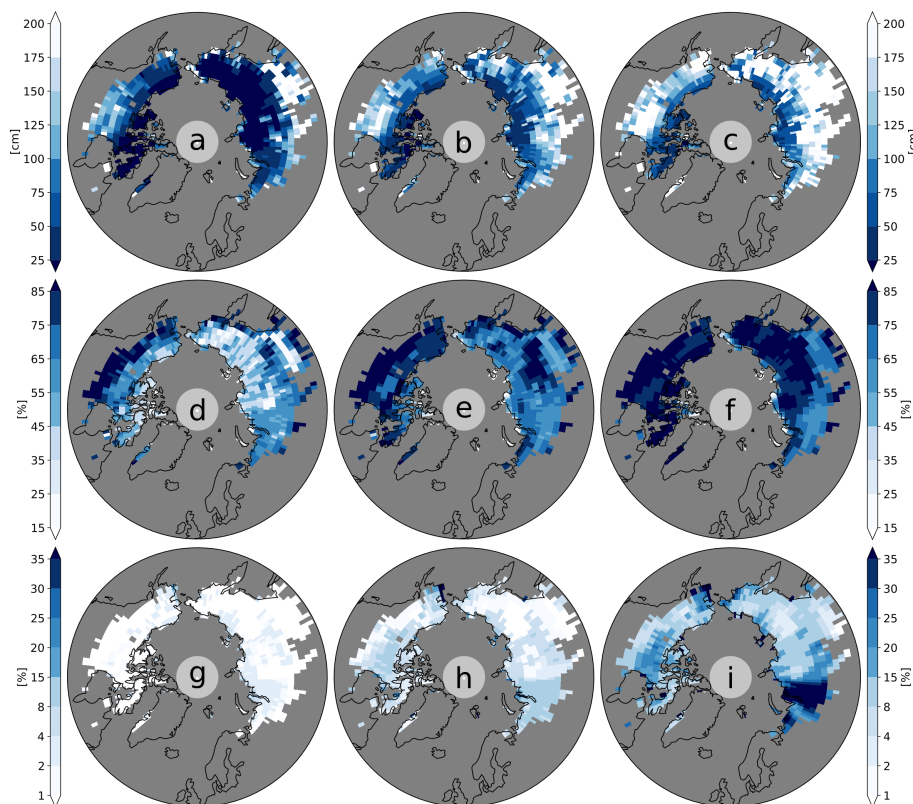
Figure 2. Simulated permafrost, vegetated fraction and inundated areas in the year 2000: a) Ensemble minimum thaw depth (annual maximum) corresponding to the year 2000 (1990 - 2010 mean). Grey areas indicate grid boxes in which the annual maximum temperatures throughout the top 3 meters of the soil exceeded the melting point for more than 10 years in the period 1990 - 2010. These are considered to be unaffected by near-surface permafrost and are not taken into consideration in the study. **b)** Same as a but for the ensemble mean. **c)** Same as a but for the ensemble maximum. **d)** Ensemble minimum vegetated fraction. Note that this is the maximum grid box fraction that can be covered by vegetation, while the actual vegetated cover depends on the current state of the vegetation and can vary throughout the year. **e)** Same as d but for the ensemble mean. **f)** Same as d but for the ensemble maximum. **g)** Annual minimum inundated fraction for the year 2000. Shown is the ensemble mean. **h)** Same as g but for the annual mean. **i)** Same as g but for the annual maximum inundated fraction.
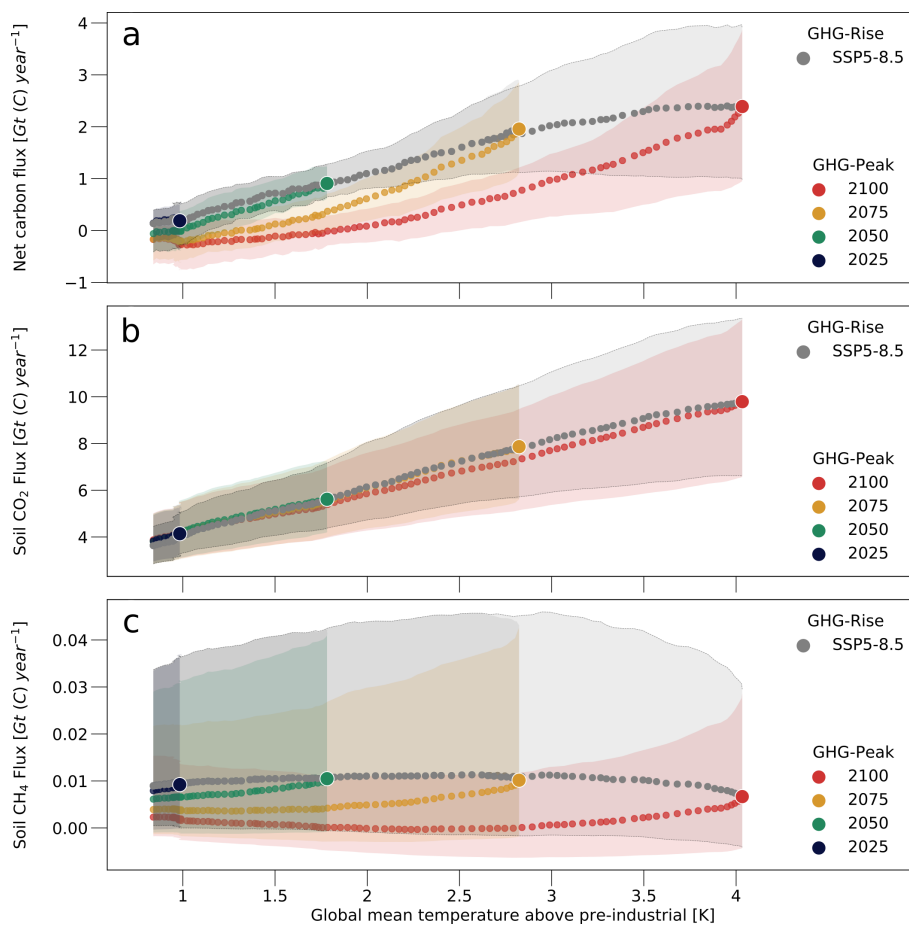
Figure 3. Net ecosystem carbon flux, soil CO₂ flux and soil methane emissions in permafrost-affected areas: a) Simulated net CO_2 flux into the atmosphere, taking into account heterotrofic and autotrophic respiration, disturbances, land-use emissions and the CO_2 uptake by plants. **b)** Same as a but showing the soil CO_2 emissions. **c)** Same as a but showing the soil (net) methane flux. Grey dots show the ensemble mean increase in CO_2 emissions as a function of the temperature increase according to the SSP5-RCP8.5 scenario. Coloured dots indicate the ensemble mean decline in CO_2 fluxes for the reversion of the forcing after a forcing-peak in 2025 (blue), 2050 (green), 2075 (yellow) and 2100 (red). Each dot represents a 20 year (moving) average. Shaded areas indicate the spread between the ensemble minimum and maximum. The figure is representative of those areas that were affected by near-surface permafrost in the year 2000.
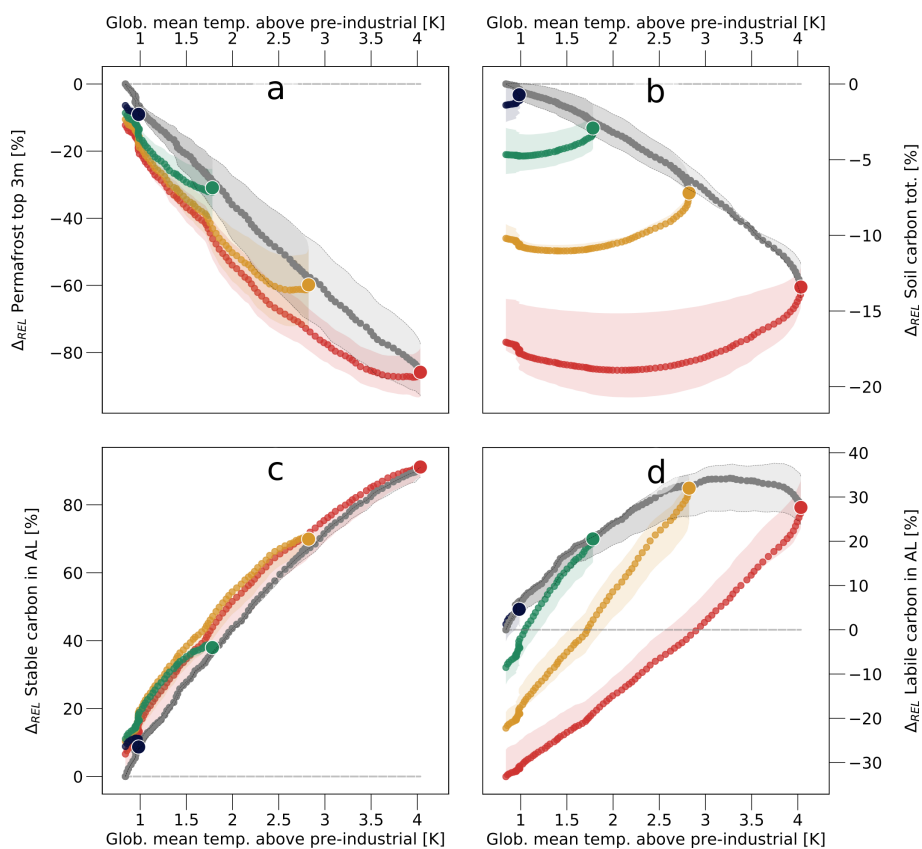
Figure 4. Permafrost and soil carbon: a) Changes in the volume of near-surface permafrost relative to the permafrost volume at the beginning of the 21st century **b)** Same as a but for the relative change in total soil carbon. **c)** Same as a but for the stable carbon within the active layer. **d)** Same as a but for the labile carbon within the active layer. The figure is representative of those areas that were affected by near-surface permafrost in the year 2000. Colours and symbols have the same meaning as in figure 3.
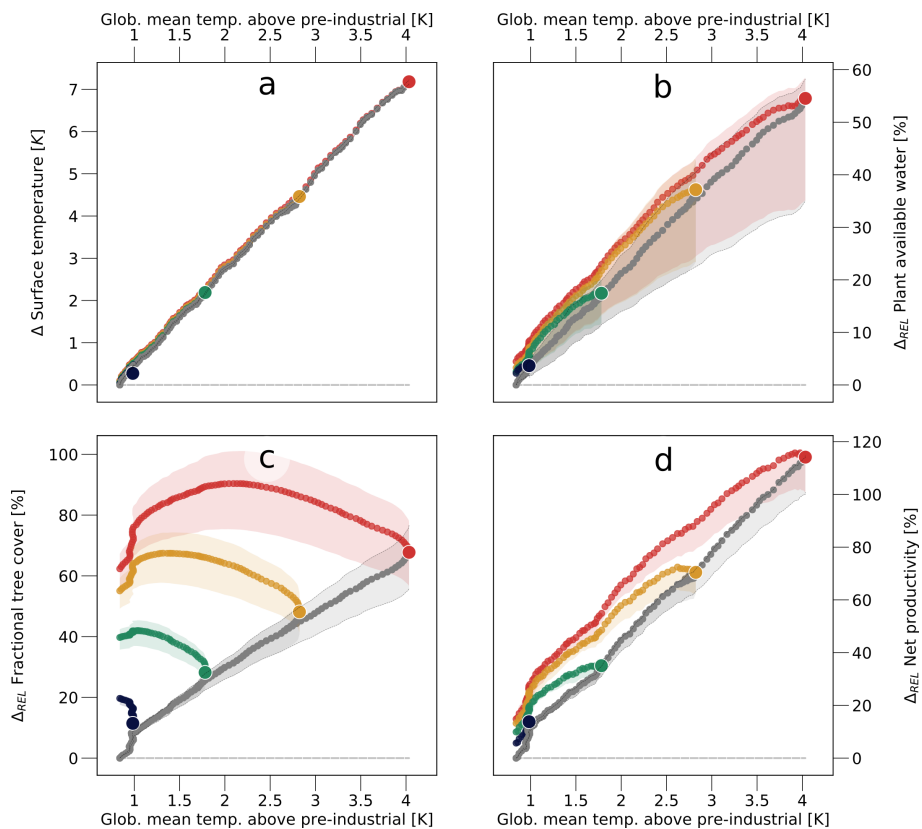
Figure 5. Drivers of soil carbon inputs: a) Change in mean surface temperature. Relative change in: **b)** Plant available water. **c)** Tree cover. **d)** Net primary productivity. All sub-figures pertain to regions with permafrost-affected soils. Colours and symbols have the same meaning as in figure 3.
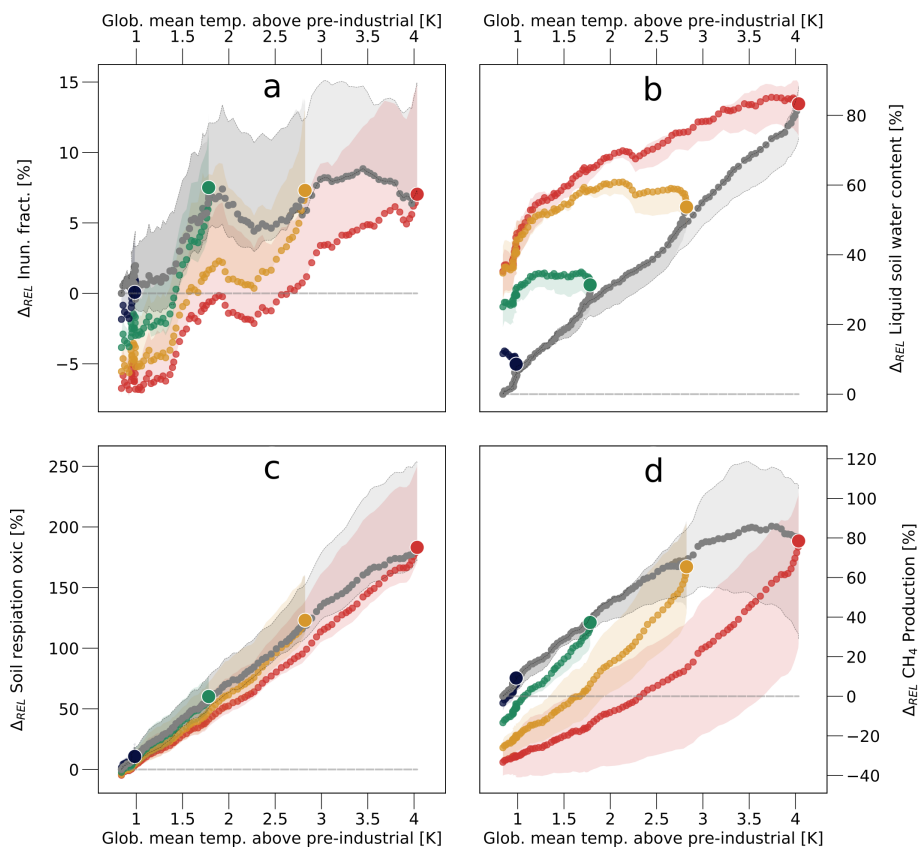
Figure 6. Soil CH$_4$ and CO$_2$ production in seasonally inundated areas: Relative change in: **a)** Extent of inundated areas. **b)** Liquid water content of the soil. **c)** Oxic soil respiration. **d)** Soil methane production. Sub-figure a shows the simple spatial average over permafrost-affected grid boxes, while sub-figures b-d include a weighting by the (annual-mean) wetland fraction. Colours and symbols have the same meaning as in figure 3.
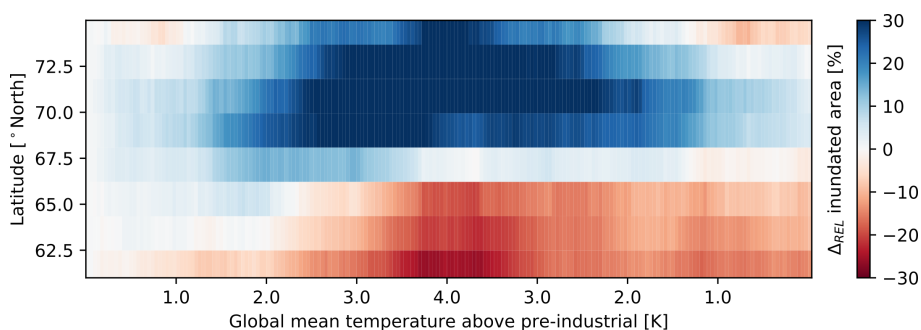
Figure 7. Wetland area in permafrost-affected regions: Relative change in the inundated area as a function of latitude and (global mean) temperature change.
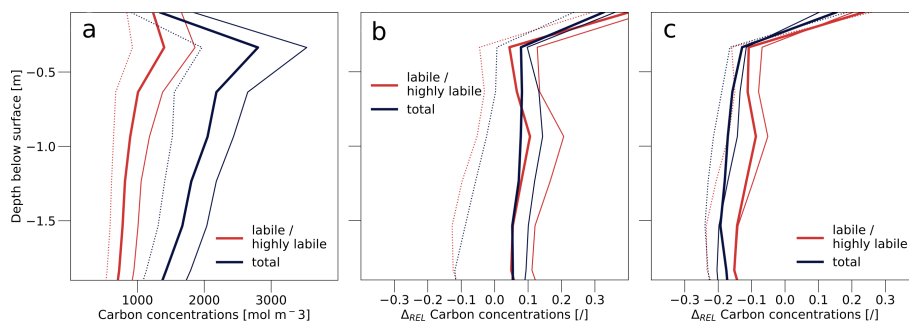
Figure 8. Soil carbon profiles in seasonally inundated areas: a) Carbon concentration as a function of soil depth in the year 2000 (1990 - 2010 average). Red lines show the concentration of labile and highly labile organic matter while blue lines represent the total carbon concentration. Thick solid lines show the ensemble mean, while dotted lines indicate the ensemble minimum and thin solid lines the ensemble maximum. **b)** Relative change in soil carbon concentrations between the forcing peak in the year 2100 (2090 - 2110 average) and the year 2000 (1990 - 2010 average). **c)** Same as b, but showing the differences between the years 2200 – when the forcing is fully reversed after a GHG peak in the year 2100 – and 2000. All sub-figures show the average over permafrost-affected grid boxes, weighted by their (annual-mean) wetland fraction.
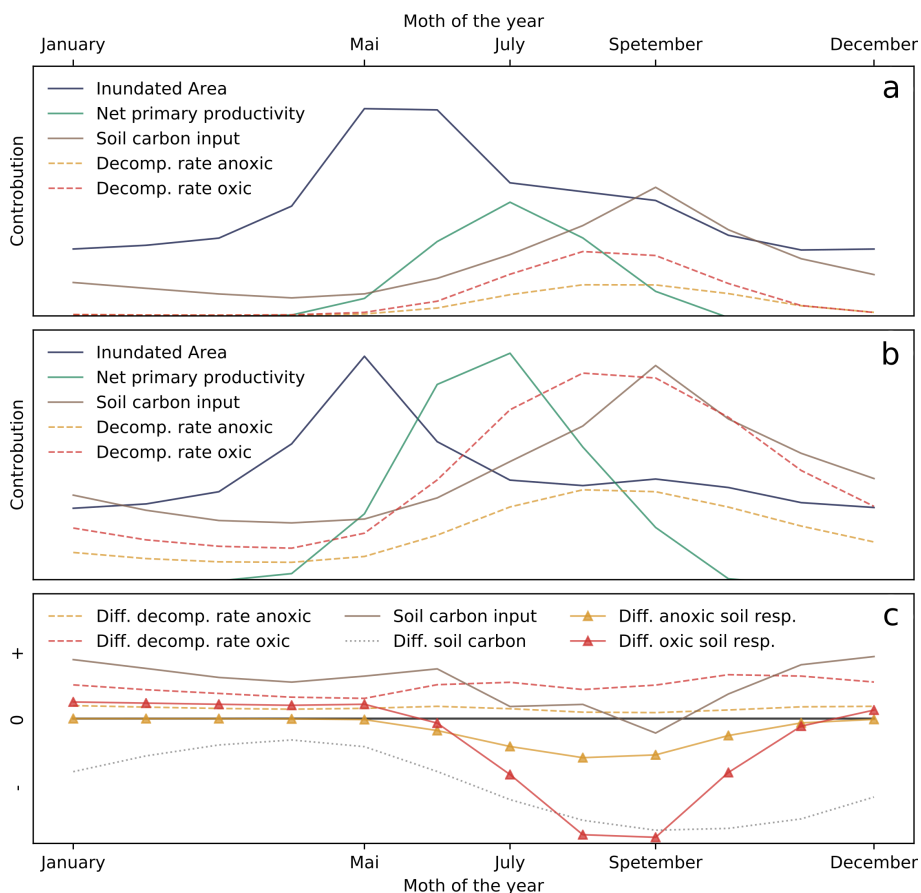
Figure 9. Seasonal dynamics in inundated areas: a) Annual cycle of inundated areas (blue lines), NPP (green), carbon input into the soil (brown), decomposition rates under anoxic conditions (yellow) and under oxic conditions (red) in permafrost-affected regions that feature a large wetland extent. Shown (qualitatively) are the seasonal dynamics that are representative for the year 2000, before the increase in atmospheric GHG concentrations. **b)** Same as a, but representative for a given forcing peak. **c)** (Qualitative) Differences in anoxic (dashed yellow lines) and oxic (red dashed lines) decomposition rates, carbon input into the soil (solid brown line), organic matter within the active layer (dotted grey line), anoxic (solid yellow line) and oxic soil respiration rates (solid red line) after and before a given forcing peak.
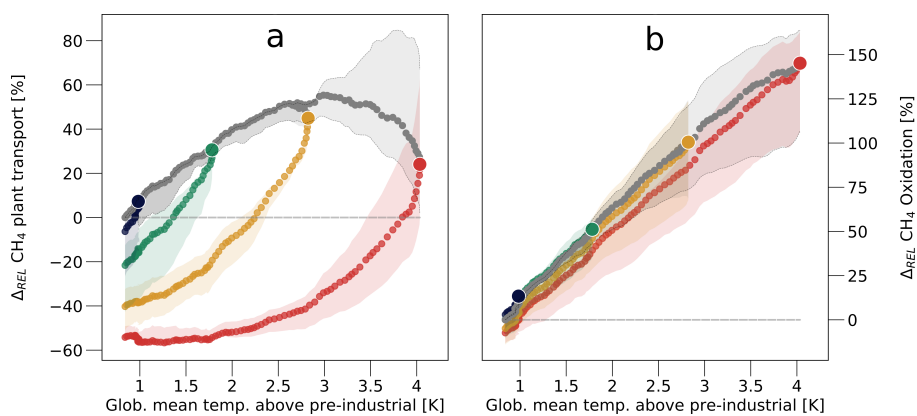
Figure 10. Methane transport: Relative change in: **a)** Amount of methane that is taken up by roots and emitted at the surface. **b)** Amount of methane that is oxidised within the soil. Colours and symbols have the same meaning as in figure 3.

Table 1. Overview over key variables in regions affected by near-surface permafrost. The first half of the table (2000,2025,2050,2075,2100) represents pools, states and fluxes during the increase in GHG concentrations according to the SSP5-RCP8.5 scenario. The second half represents the post-peak (pp) pools, fluxes and states when the forcing has been fully reversed. 2050pp refers to the year 2050 after a GHG peak in the year 2025, 2100pp to a peak in 2050, 2150pp to the peak in 2075 and 2200pp to a peak in the year 2100. Black numbers indicate the ensemble mean and the grey number in brackets indicate the ensemble minimum and maximum. All variables represent simple spatial averages over the region affected by near-surface permafrost and averages over a 20-year period.

Varibale	Unit	2000	2025	2050	2075	2100	2050pp	2100pp	2150pp	2200pp
Soil carbon tot.	[Gt(C)]	1098	1090	1066	1019	951	1083	1047	986	911
		(820/1377)	(807/1376)	(788/1353)	(756/1288)	(722/1182)	(799/1376)	(771/1337)	(735/1249)	(703/1134)
Highly labile carbon in AL	[Gt(C)]	45.3	48.0	52.1	54.1	48.0	44.9	42.4	39.0	36.7
		(28.8/66.7)	(30.1/72.4)	(32.2/79.7)	(32.6/87.2)	(32.1/77.4)	(28.3/68.6)	(27.4/65.5)	(26.9/58.0)	(27.2/50.4)
Labile carbon in AL	[Gt(C)]	149.5	163.7	183.8	200.3	190.8	152.6	137.8	117.1	100.4
		(108.0/186.6)	(114.6/205.3)	(127.8/230.0)	(137.0/255.3)	(133.6/251.1)	(106.2/191.0)	(95.5/174.1)	(84.5/152.8)	(79.2/125.1)
Stable carbon in AL	[Gt(C)]	303.2	349.0	428.3	523.8	579.5	332.7	339.7	337.4	326.2
		(238.9/367.8)	(271.8/426.2)	(335.9/517.8)	(407.2/633.4)	(449.2/692.5)	(257.5/404.9)	(259.2/412.3)	(253.7/406.6)	(244.9/388.0)
Net carbon flux	[Gt(C) $year^{-1}$]	0.14	0.4	1.02	2.04	2.39	0.19	-0.02	-0.13	-0.14
		(-0.41/0.39)	(0.03/0.77)	(0.74/1.43)	(1.14/3.13)	(0.98/3.91)	(-0.19/0.43)	(-0.38/0.21)	(-0.53/0.09)	(-0.61/0.14)
Net primary productivity	[Gt(C) $year^{-1}$]	3.69	4.32	5.23	6.62	7.9	3.91	4.07	4.2	4.26
		(2.84/5.03)	(3.32/5.83)	(4.04/6.94)	(5.1/8.58)	(6.1/10.1)	(2.97/5.3)	(3.02/5.59)	(3.08/5.83)	(3.1/5.95)
Soil CO_2 flux	[Gt(C) $year^{-1}$]	3.64	4.48	5.95	8.2	9.8	3.88	3.86	3.87	3.92
		(2.85/4.45)	(3.57/5.65)	(4.61/7.73)	(6.0/11.2)	(6.6/13.3)	(2.99/5.0)	(2.89/5.05)	(2.87/5.04)	(2.89/5.07)
Soil CH_4 flux	[Mt(C) $year^{-1}$]	9.0	9.9	11.0	11.2	6.7	8.1	6.2	4.0	2.3
		(0.5/33.7)	(-0.1/38.1)	(-0.8/43.9)	(-1.5/45.6)	(-4.1/29.5)	(-0.3/33.9)	(-0.9/29.3)	(-1.3/21.9)	(-1.7/15.4)
Soil methane production	[Mt(C) $year^{-1}$]	23.5	27.4	34.3	42.1	42.2	23.2	21.0	18.0	15.9
		(14.0/49.2)	(15.5/56.9)	(20.6/67.9)	(28.6/76.5)	(27.9/63.6)	(12.9/50.2)	(11.7/44.9)	(10.8/36.3)	(10.5/29.7)
CH_4 plant transport	[Mt(C) $year^{-1}$]	10.9	12.4	15.0	16.9	13.5	10.3	8.6	6.6	5.0
		(2.8/34.7)	(2.8/39.7)	(3.7/46.9)	(4.5/50.4)	(4.7/35.5)	(2.1/35.0)	(1.6/30.8)	(1.4/23.7)	(1.3/17.7)
CH_4 oxidation	[Mt(C) $year^{-1}$]	14.5	17.5	23.2	30.9	35.6	15.1	14.7	14.0	13.6
		(9.7/23.4)	(11.4/27.9)	(16.1/35.0)	(23.0/42.9)	(25.6/48.3)	(10.2/22.5)	(10.0/21.3)	(9.5/20.4)	(8.8/20.5)
Soil temp. at 1m	[K]	267.5	268.4	270.1	272.3	274.2	267.9	268.1	268.2	268.3
		(267.0/267.8)	(267.9/268.7)	(269.6/270.4)	(271.9/272.7)	(273.9/274.6)	(267.5/268.2)	(267.7/268.4)	(267.8/268.6)	(268.0/268.7)
Permafrost in top 3m	[m]	1.98	1.73	1.31	0.74	0.28	1.83	1.79	1.75	1.71
		(1.73/2.27)	(1.46/2.06)	(0.98/1.7)	(0.42/1.12)	(0.12/0.51)	(1.58/2.14)	(1.54/2.1)	(1.52/2.06)	(1.49/2.03)
Inundated fract. (mean)	[%]	5.48	5.54	5.9	5.95	5.88	5.44	5.33	5.23	5.16
		(4.23/6.53)	(4.42/6.46)	(4.81/6.84)	(4.89/7.1)	(4.63/7.45)	(4.27/6.44)	(4.16/6.4)	(4.11/6.3)	(3.97/6.26)